Journal of Geophysical Research: Atmospheres

RESEARCH ARTICLE
10.1029/2017JD028250

This article is a companion to Bossert et al. (2018) https://doi.org/10.1029/2018JD028319.

Key Points:
- Weak orographic forcing and conducive propagation conditions at lower altitudes can yield large mountain wave amplitudes in the mesosphere
- Mesospheric mountain waves can extend over 1,000 km around the source terrain and persist for many hours after forcing ceases
- Mesospheric mountain waves having {lambda}$_h$ < 100 km can achieve very large momentum fluxes and exhibit strong overturning and instabilities

Supporting Information:
- Movie S1
- Supporting Information S1

Correspondence to:
D. C. Fritts,
dave@gats-inc.com

Citation:
Fritts, D. C., Vosper, S. B., Williams, B. P., Bossert, K., Plane, J. M. C., Taylor, M. J., et al. (2018). Large-amplitude mountain waves in the mesosphere accompanying weak cross-mountain flow during DEEPWAVE Research Flight RF22. *Journal of Geophysical Research: Atmospheres*, *123*, 9992–10,022. https://doi.org/10.1029/2017JD028250

Received 28 DEC 2017
Accepted 5 JUL 2018
Accepted article online 3 AUG 2018
Published online 17 SEP 2018

Author Contributions

Conceptualization: David C. Fritts
Formal analysis: David C. Fritts, Simon B. Vosper, John M. C. Plane, Stephen D. Eckermann, John M. C. Plane, Stephen D. Eckermann
(continued)

Large-Amplitude Mountain Waves in the Mesosphere Accompanying Weak Cross-Mountain Flow During DEEPWAVE Research Flight RF22

David C. Fritts[1], Simon B. Vosper[2], Bifford P. Williams[1], Katrina Bossert[1], John M. C. Plane[3], Michael J. Taylor[4], P.-Dominique Pautet[4], Stephen D. Eckermann[5], Christopher G. Kruse[6], Ronald B. Smith[6], Andreas Dörnbrack[7], Markus Rapp[7], Tyler Mixa[1], Iain M. Reid[8], and Damian J. Murphy[9]

[1]GATS Inc., Boulder, CO, USA, [2]Met Office, Exeter, UK, [3]School of Chemistry, University of Leeds, Leeds, UK, [4]Department of Physics, Utah State University, Logan, UT, USA, [5]Space Science Division, U.S. Naval Research Laboratory, Washington, DC, USA, [6]Department of Geology and Geophysics, Yale University, New Haven, CT, USA, [7]German Aerospace Center, Munich, Germany, [8]Department of Physics, University of Adelaide, Adelaide, South Australia, Australia, [9]Australian Antarctic Division, Kingston, Tasmania, Australia

Abstract Mountain wave (MW) propagation and dynamics extending into the upper mesosphere accompanying weak forcing are examined using in situ and remote-sensing measurements aboard the National Science Foundation/National Center for Atmospheric Research Gulfstream V (GV) research aircraft and the German Aerospace Center Falcon. The measurements were obtained during Falcon flights FF9 and FF10 and GV Research Flight RF22 of the Deep Propagating Gravity Wave Experiment (DEEPWAVE) performed over Mount Cook, New Zealand, on 12 and 13 July 2014. In situ measurements revealed both trapped lee waves having zonal wavelengths of λ_x ~ 12 km and less, and larger-scale, vertically propagating MWs primarily at λ_x ~ 20–60 km and ~100–300 km extending from west to ~400 km east of Mount Cook. GV Rayleigh lidar measurements from 25- to 60-km altitudes showed that the weak forcing and zonal winds that increased from ~12 m/s at 12 km to ~40 and 130 m/s at 30 and 55 km, respectively, enabled largely linear MW propagation and strong amplitude growth with altitude into the mesosphere. GV Na lidar and airglow imager measurements revealed an extensive MW response from ~70 to 87 km with large amplitudes and vertical displacements at λ_x ~ 40–300 km but with both decreasing with altitude approaching a critical level near 90 km. These MWs exhibited large-scale MW breaking and among the largest sustained momentum fluxes observed in the mesosphere. UK Met Office Unified Model simulations of the RF22 MW event captured many aspects of the observed MW field and revealed that despite the dominant large-scale MW responses in the stratosphere, the major momentum fluxes accompanied smaller-scale waves.

1. Introduction

Gravity waves (GWs) contribute significantly to the structure and variability of the atmosphere over a wide range of spatial and temporal scales from the surface into the thermosphere. Their importance derives from their many sources, ubiquity (they are virtually always present), diverse interactions, major contributions to energy and momentum transport, and generation of instabilities and turbulence that account for local energy and momentum deposition (see reviews of these dynamics by Staquet & Sommeria, 2002; Fritts & Alexander, 2003; Sutherland, 2010; Nappo, 2002; and Bühler, 2014).

Multiple processes are now understood to excite GWs having a wide range of scales throughout the atmosphere. Important sources at lower altitudes include orography, deep convection, jet streams, and frontal systems. Orographic GWs, or mountain waves (MWs), arise wherever there is significant terrain, have spatial scales dictated by the terrain scales and cross-mountain flows, and can have both upstream and downstream influences. The horizontal scales that readily achieve higher altitudes can be as small as ~10–20 km and as large as ~200 km or larger, but their dynamics and ability to propagate to higher altitudes depend strongly on the intervening wind and stability profiles and whether these dynamics are linear or nonlinear (e.g., Bramberger et al., 2017; Durran, 1990; Grubišić et al., 2008; Klemp & Lilly, 1978; Lilly & Kennedy, 1973; Lilly & Lester, 1974; Nastrom & Fritts, 1992; Shutts & Vosper, 2011; R. B. Smith et al., 2008; Vosper, 2015; Vosper et al., 2016). Where strong zonal winds extend into the stratosphere, orographic sources lead to the

Funding acquisition: David C. Fritts, Markus Rapp, Markus Rapp
Investigation: David C. Fritts, Simon B. Vosper, Bifford P. Williams, Katrina Bossert, Michael J. Taylor, P.-Dominique Pautet, Stephen D. Eckermann, Christopher G. Kruse, Michael J. Taylor, P.-Dominique Pautet, Stephen D. Eckermann, Christopher G. Kruse, Ronald B. Smith, Andreas Dörnbrack, Tyler Mixa, Iain M. Reid, Christopher G. Kruse, Ronald B. Smith, Andreas Dörnbrack, Tyler Mixa, Iain M. Reid, Damian J. Murphy
Methodology: David C. Fritts, Bifford P. Williams, Katrina Bossert, John M. C. Plane, Michael J. Taylor, P.-Dominique Pautet, Stephen D. Eckermann, Christopher G. Kruse, John M. C. Plane, Michael J. Taylor, P.-Dominique Pautet, Stephen D. Eckermann, Christopher G. Kruse, Ronald B. Smith, Andreas Dörnbrack, Iain M. Reid, Christopher G. Kruse, Ronald B. Smith, Andreas Dörnbrack, Iain M. Reid, Damian J. Murphy
Supervision: David C. Fritts
Visualization: Simon B. Vosper, P.-Dominique Pautet, Christopher G. Kruse, P.-Dominique Pautet, Christopher G. Kruse, Christopher G. Kruse
Writing - original draft: David C. Fritts
Writing – review & editing: David C. Fritts

middle- to high-latitude GW *hot spots* identified in high-resolution satellite radiance data (e.g., Eckermann & Preusse, 1999; Hendricks et al., 2014; Jiang et al., 2003; Wu & Eckermann, 2008).

Deep convection yields GWs that have similar horizontal scales to MWs but often more nearly isotropic propagation and responses at higher altitudes, depending on the character of the source and propagation environments (e.g., Fovell et al., 1992; Horinouchi et al., 2002; Lane et al., 2001; Pfister et al., 1993; Yue et al., 2009). While deep convection can occur in many regions, preferred locations such as the Intertropical Convergence Zone and major cyclones such as hurricanes contribute most to the global statistics seen in satellite radiance and GPS data and modeled responses in these regions (e.g., Liu et al., 2014; Tsuda et al., 2000). Frontal systems and jet streams are likewise significant sources of GWs but often at larger scales than typically arise from orography and deep convection (Fritts & Nastrom, 1992; Guest et al., 2000; Hirota & Niki, 1985; Plougonven & Snyder, 2007; Plougonven & Zhang, 2014; Thomas et al., 1992; Uccellini & Koch, 1987; Zhang, 2004). Of these sources, orography and convection often lead to GWs having larger intrinsic frequencies, ω_i, whereas frontal systems and jet streams more typically yield smaller ω_i due to their larger horizontal-to-vertical wavelength ratios.

The influences of these various GWs depend on their amplitudes, momentum fluxes, and propagation to higher altitudes. Those having larger vertical group velocities (e.g., convective and orographic GWs with larger ω_i and vertical wavelengths, λ_z) more easily penetrate to high altitudes and achieve large amplitudes and momentum fluxes. Those having smaller vertical group velocities (e.g., frontal and jet stream GWs) with smaller ω_i and λ_z can nevertheless penetrate to high altitudes and achieve large amplitudes under suitable propagation conditions. However, their momentum fluxes are typically smaller because of their larger horizontal scales (see, e.g., Fritts & Alexander, 2003; Plougonven & Zhang, 2014).

GWs that achieve large amplitudes and momentum fluxes often induce strong wave-wave interactions, wave/mean-flow interactions, and/or local instabilities and turbulence that act as sources of additional GWs. Wave-wave interactions yield energy transfers among modes within the GW spectrum that can couple very different scales without dissipation, drive the GW field toward an equilibrium spectrum, and compete with local instabilities in reducing primary GW amplitudes (e.g., Dong & Yeh, 1988; Dunkerton, 1989; Fritts et al., 2013; Fritts, Wang, et al., 2016; Grimshaw, 1988; Hines, 1991; Huang et al., 2007, 2009, 2011; Klostermeyer, 1991; McComas & Bretherton, 1977; Sonmor & Klaassen, 1997; Vanneste, 1995; Yeh & Liu, 1981).

Momentum transport by GW packets localized in one, two, or three dimensions (1-D, 2-D, or 3-D) can induce local mean flow accelerations that have several effects. One-dimensional localization (in altitude or time) induces distortions of the GW phase structure due to *self-acceleration* dynamics or modulational instabilities at sufficiently high ω_i (Dosser & Sutherland, 2011; Fritts et al., 2015; Sutherland, 2006a, 2006b).

Induced mean flows due to localization of large-amplitude GWs in 2-D or 3-D yield strong forcing of secondary GWs having scales and orientations dictated by the packet scales of the initial GW (Vadas, 2007; Vadas & Fritts, 2001). Secondary GWs that are excited at larger vertical scales can propagate to much higher altitudes because of their much larger horizontal phase speeds and vertical group velocities than the primary GWs. Importantly, secondary generation due to local GW momentum transport often precedes the occurrence of instabilities and dissipation (e.g., Fritts et al., 2015), in contrast to the assumption in earlier analytic studies of these dynamics (Vadas, 2007; Vadas & Fritts, 2001).

Secondary GWs can also arise at scales comparable to, or smaller than, the initial GW due to various local GW instability dynamics that arise in idealized or multiscale environments. Important classes include self-acceleration instabilities, GW breaking, Kelvin-Helmholtz instabilities, and intrusion events that can have various orientations relative to the plane of GW propagation (e.g., Dunkerton, 1989; Fritts et al., 2009a; Fritts et al., 2013; Fritts, Wang, et al., 2016; Fritts et al., 2017; Fritts & Rastogi, 1985; Lelong & Dunkerton, 1998; Lombard & Riley, 1996; Sonmor & Klaassen, 1997). These instabilities can lead to additional GW generation at the instability scales (e.g., Bühler et al., 1999; Chimonas & Grant, 1984; Fritts, 1984; Scinocca & Ford, 2000).

Thus, there is considerable evidence for important GW interactions, instability dynamics, and transports throughout the atmosphere. Indeed, many insights into these dynamics in the troposphere and lower stratosphere have come from parallel measurements and modeling efforts, often focused on MWs due to their known locations (see overview papers by Bougeault et al., 2001; Grubišić & Lewis, 2004; R. B. Smith et al., 2007; Grubišić et al., 2008; Fritts, Smith, et al., 2016). Until recently, however, there have been no observations

that have simultaneously quantified GW amplitudes, horizontal and vertical scales, propagation, and instability dynamics from their sources at lower altitudes to their regions of dissipation at higher altitudes.

The first program to do so was the Deep Propagating Gravity Wave Experiment (DEEPWAVE), which employed new remote-sensing instruments aboard the National Science Foundation/National Center for Atmospheric Research Gulfstream V (GV) research aircraft and was performed over and around New Zealand (NZ) during June and July 2014. DEEPWAVE also employed the German DLR Falcon research aircraft and extensive ground-based instrumentation on the NZ South Island (SI) and Tasmania (Fritts, Smith, et al., 2016). These data are enabling multiple studies of various GW dynamics from the surface to ~100 km (e.g., Bossert et al., 2015, 2017; Bramberger et al., 2017; Eckermann et al., 2016; Heale et al., 2017; Kaifler et al., 2015; Kruse & Smith, 2015; Pautet et al., 2016; R. B. Smith et al., 2016).

DEEPWAVE airborne measurements were performed during austral winter in order to address mountain wave responses extending to high altitudes in a strong zonal wind environment and to avoid the potential for cessation of deep MW propagation by a stratospheric sudden warming. NZ was chosen as the primary research target given that this is a major Southern Hemisphere hotspot of GW activity in satellite measurements in the stratosphere that was easily accessed from the Christchurch airport, which has excellent support facilities. Existing ground-based instruments on SI were supplemented with additional radars, balloons, lidars, and airglow imagers on SI and Tasmania, most of which began observations prior to flight operations and several that continued months beyond flight operations. An overview of the DEEPWAVE program, the various aircraft and ground-based instruments, the various research flights, and examples of significant results and key findings was provided by Fritts, Smith, et al. (2016).

Our goal in this paper is to describe the MW dynamics observed on Research Flight 22 (RF22), which examined the structure and evolution of MW responses to weak flow across the SI terrain. RF22 proved to be an interesting case, with weak MW forcing and a mean wind environment that enabled largely linear propagation and strong amplitude growth into the upper stratosphere and lower mesosphere. This yielded very large MW amplitudes, vertical displacements, and momentum fluxes in the mesosphere, followed by strong breaking below a critical level near 90 km and excitation of secondary GWs propagating to higher altitudes (Bossert et al., 2017).

Section 2 defines the parameters to be discussed and the relations between them in varying wind and temperature (or stability) profiles. Section 3 describes DEEPWAVE flight planning, meteorological conditions, and the background fields during 12 and 13 July as defined by ground-based measurements, radiosondes, Sounding of the Atmosphere using Broadband Emission Radiometry (SABER) aboard the Thermosphere, Ionosphere, Mesosphere Energetics Dynamics satellite, the European Centre for Medium-Range Weather Forecasts (ECMWF) Integrated Forecasting System, and the NAVy Global Environment Model (NAVGEM) reanalyses. Flight-level MW fields, scales, and momentum fluxes defined by Falcon and GV flights on 12 and 13 July are described in section 4. Sections 5 and 6, respectively, describe stratospheric and mesospheric MWs and possible other GWs as seen by the GV lidars and airglow instruments. Section 7 describes UK Met Office Unified Model (UM) simulations performed for comparisons with RF22 measurements and to assess resolution impacts on the MW fields and momentum fluxes. The implications of these results for MW propagation, momentum fluxes, and forcing at higher altitudes, and their relation to previous measurements, are described in section 8. Section 9 presents our summary and conclusions.

2. GW Parameters and Relations

Given the diverse measurements we employ in this study, and our desire to infer MW and more general GW characteristics, scales, amplitudes, and likelihood of wave breaking, we summarize here the relations among GW and mean parameters dictated by the equations of motion. For this purpose, we assume that motions are linear, inviscid, Boussinesq, and 2-D (no Coriolis force) in a vertical plane along the direction of MW propagation and that mean fields are uniform horizontally and slowly varying in altitude. Then the total wind, temperature, potential temperature, pressure, and density fields, (u,v,w), T, θ, p, and ρ, may be written as $\phi\ (x,y,z,t) = \phi_0(z,t) + \phi'(x,y,z,t)$, with $\phi'(x,z,t) = \phi' \exp\,[i\,(kx + ly + mz - \omega t)]$, where the subscript 0 and primes denote mean and perturbation quantities, $u_0 = U$, $v_0 = V$, ϕ' grows as $e^{z/2H}$ for scale height H, with respect to the mean quantities for T, θ, p, and ρ for conservative motions, and eastward u' and U, northward v', and upward w' are positive. Additionally, GW horizontal and vertical wavenumbers and wavelengths are related by $|k| = 2\pi/\lambda_x$,

$|l| = 2\pi/\lambda_y$, and $|m| = 2\pi/\lambda_z$, with the sign convention that $k > 0$, $l > 0$, and $m < 0$ for eastward, northward, and upward GW propagation. Additionally, the intrinsic and ground-based GW frequencies are related by $\omega_i = \omega - k_h U_h = k_h\,(c - U_h) = k_h c_i$. Here $|k_h| = (k^2 + l^2)^{1/2}$, $|u_h'| = (u'^2 + v'^2)^{1/2}$, U_h, c, and c_i are the GW horizontal wavenumber and velocity perturbation, mean wind, and GW horizontal phase speed and intrinsic phase speed along k_h. The local buoyancy frequency squared is $N^2(z) = (g/\theta)(\mathrm{d}\theta/\mathrm{dz})$, with mean ${N_0}^2(z)$ for $\theta = \theta_0$, g is gravitational acceleration, and $\lambda_z \ll 4\pi H$, except where ω_i approaches N due to increasing $|c - U|$ or decreasing N.

Useful relations obtained with the above assumptions include the following:

$$ku' + lv' + mw' = 0, \tag{1}$$

$$p' = -\rho_0\left({N_0}^2 - {\omega_i}^2\right)w'/m\omega_i = \rho_0\omega_i {u_h}'/k_h \tag{2}$$

$$\theta'/\theta_0 = -iN_0{}^2w'/g\omega_i = iN_0{}^2{u_h}'/g\,\left(N_0{}^2 - \omega_i{}^2\right)^{1/2} \tag{3}$$

For hydrostatic GWs (i.e., $k^2 \ll m^2$), we also obtain the following:

$$\lambda_z = 2\pi(c - U_h)/N_0 \tag{4}$$

$$|\,{u_h}'\,| = (g/N_0)\,|\,T'/T_0\,| \tag{5}$$

$$|\,\mathrm{d}{u_h}'/\mathrm{dz}\,| = |\,m{u_h}'\,| = aN_0, \text{where } a = |\left(\mathrm{d}\theta'/\mathrm{dz}\right)|/(\mathrm{d}\theta_0/\mathrm{dz}) = |\,{u_h}'/(c - U_h)\,| \tag{6ab}$$

Here $a = 1$ is the nondimensional GW amplitude at which insipient overturning occurs, hence near which wave breaking and instabilities are likely to arise (e.g., Fritts et al., 2009a, 2009b).

Vertical energy (*EF*) and momentum (*MF*) fluxes along Falcon flights 9 and 10 (FF9 and FF10), and GV Research Flight 22 (RF22) flight tracks are related for linear, steady MW flows and may be written as follows (Eliassen & Palm, 1961; R. B. Smith et al., 2016), where angle brackets denote averages over the appropriate MW phases:

$$MF = \rho < u'w' > \tag{7}$$

$$EF = < p'w' > = \rho N_0 < u'w' > /m = U\,MF \tag{8}$$

Another useful relation for general GWs is

$$c_{gz} = (\omega_i/m)\left(1 - {\omega_i}^2/{N_0}^2\right) \tag{9}$$

where c_{gz} is GW vertical group velocity. Finally, m is real (imaginary) for vertically propagating (evanescent) GWs, implying different relative phases in equation (1) in the two cases.

3. Flight Planning, Meteorological Conditions, and Background Fields

3.1. Flight Planning

Forecasts by the various global and mesoscale models employed for DEEPWAVE flight planning (see Fritts, Smith, et al., 2016, Table 3) anticipated moderate to strong winds (~10–20 m/s) below 700 hPa over the central SI early on 12 July with significant weakening later on 12 July and into 13 July (all in universal time, UT). At this late stage in the DEEPWAVE field program, most RFs targeting MW responses had occurred when MW forcing was relatively strong (especially RF9, 10, 12, 13, and 16; see Figure 1 at left). However, ground-based instruments at Lauder had observed very strong MW responses at ~70–90 km on 21 June when MW forcing was expected to also be very weak (see, e.g., Fritts, Smith, et al., 2016, Figure 13). Thus, the forecast conditions for 13 July were judged to be a good opportunity to explore the transition from strong to much weaker MW forcing conditions and the responses at higher altitudes. To sample this transition, the Falcon flew FF9 and FF10 with ~200-km MC2 flight legs at ~10.7 km centered at ~19:00 and 23:45 UT on 12 July. Thereafter, the GV flew RF22, comprising four ~550-km E-W MC1 flight legs at ~12 km from ~06 to 09 UT on 13 July (see Figure 1 at right).

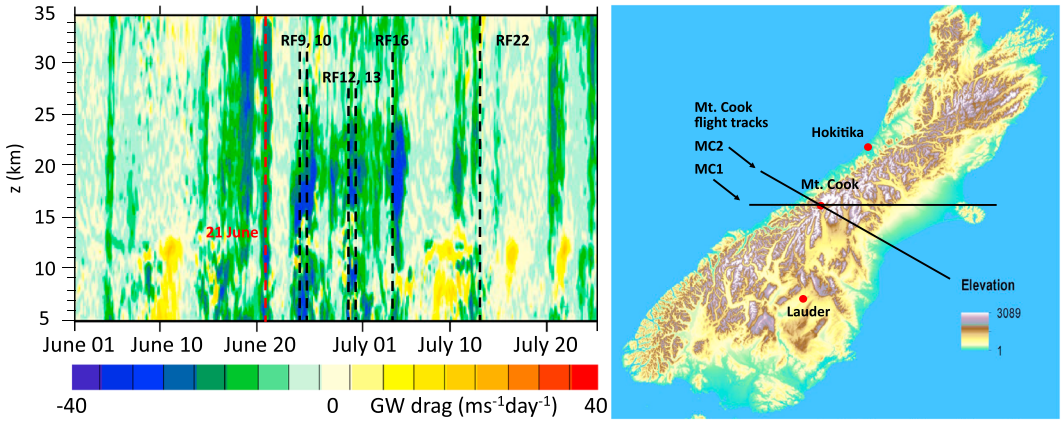

Figure 1. MW drag predicted by continuous 6-km WRF run comparing RF22 with other significant MW forcing events (left). New Zealand South Island orography and FF9, FF10, and RF22 flight tracks (right). MW = mountain wave; FF = Falcon flight; RF = Research Flight; GW = Gravity wave; WRF = Weather and Research Forecast model.

3.2. Cross-Mountain and Flight-Level Winds

Horizontal winds over SI from ECMWF operational analyses at 0.5° resolution are shown at 06 and 18 UT on 12 July and at 06 UT on 13 July at 700 and 200 hPa, respectively, in the left and middle panels of Figure 2. These confirm the forecast wind field evolution and reveal that MW forcing had largely ceased by Leg 1 of RF22. At 06 UT on 12 July, there was a pronounced low-pressure system off the SW end of SI that accounted for a significant pressure gradient at 700 hPa (see the dense geopotential height contours at 06 UT on 12 July) along SI and the strong forecast and observed winds toward the SSE at 700 and 200 hPa. This system evolved rapidly, however, and the strong pressure gradient weakened significantly by 18 UT on 12 July and even further by 06 UT on 13 July.

3.3. Radiosonde *u*, *v*, and *T* Profiles

Figures 3 and 4 display *u*, *v*, and *T* profiles obtained by nine radiosondes launched from Lauder from 11:40 on 12 July to 02:38 UT on 13 July and from Hokitika at 05 and 08 UT on 13 July. Also shown with the Hokitika radiosonde wind profiles at low altitudes in Figure 4 are hourly mean winds from the wind profiler at Hokitika spanning the full radiosonde interval.

Lauder wind profiles reveal initial, strong cross-mountain winds at 2–3 km of ~15–20 m/s toward the southeast (see the top left panels in Figures 3 and 4) that generally decreased and rotated counterclockwise thereafter. Higher in the troposphere, sustained positive *U* and increasing negative *V* with altitude and time up to ~11 km strongly favored MWs having northwest-southeast alignments with phases along the spine of the Southern Alps. See, for example, the ECMWF T' field at 200 hPa at bottom right in Figure 2, the negative correlations of larger-scale MW u' and v' in Falcon measurements at 10.7 km in Figure 6, and to a lesser degree the negative larger-scale u' and v' correlations in the GV measurements at 12 km in Figure 7.

Referring to Figure 4, we see that cross-mountain zonal winds decreased to near 0 at Lauder and Hokitika throughout 12 July and that u', v', and T' fluctuations at $\lambda_z < 5$ km likewise decreased strongly over this interval. These profiles suggest that MW forcing largely ceased during 12 July and that any MW responses at higher altitudes must have been excited at earlier times. Importantly, however, the overall decrease exhibited significant modulation, with *u* ~ 10–13, 15–18, ~10, and ~0 m/s at ~16–18, 19–21, ~24, and ~03 UT, respectively, from 12 to 13 July.

Radiosonde profiles from Lauder also revealed increasing *U* with altitude in the stratosphere from ~12–17 km and above ~25 km, and *V* increasing more uniformly above ~11 km, with *U* and *V* reaching ~50 and 10 m/s at 30 km, respectively. These winds and shears would have induced small c_i or critical levels implying dissipation and amplitude suppression for MWs propagating toward the northwest or north northwest. They also would have enabled MWs propagating toward the west and southwest with larger c_i to emerge as the dominant

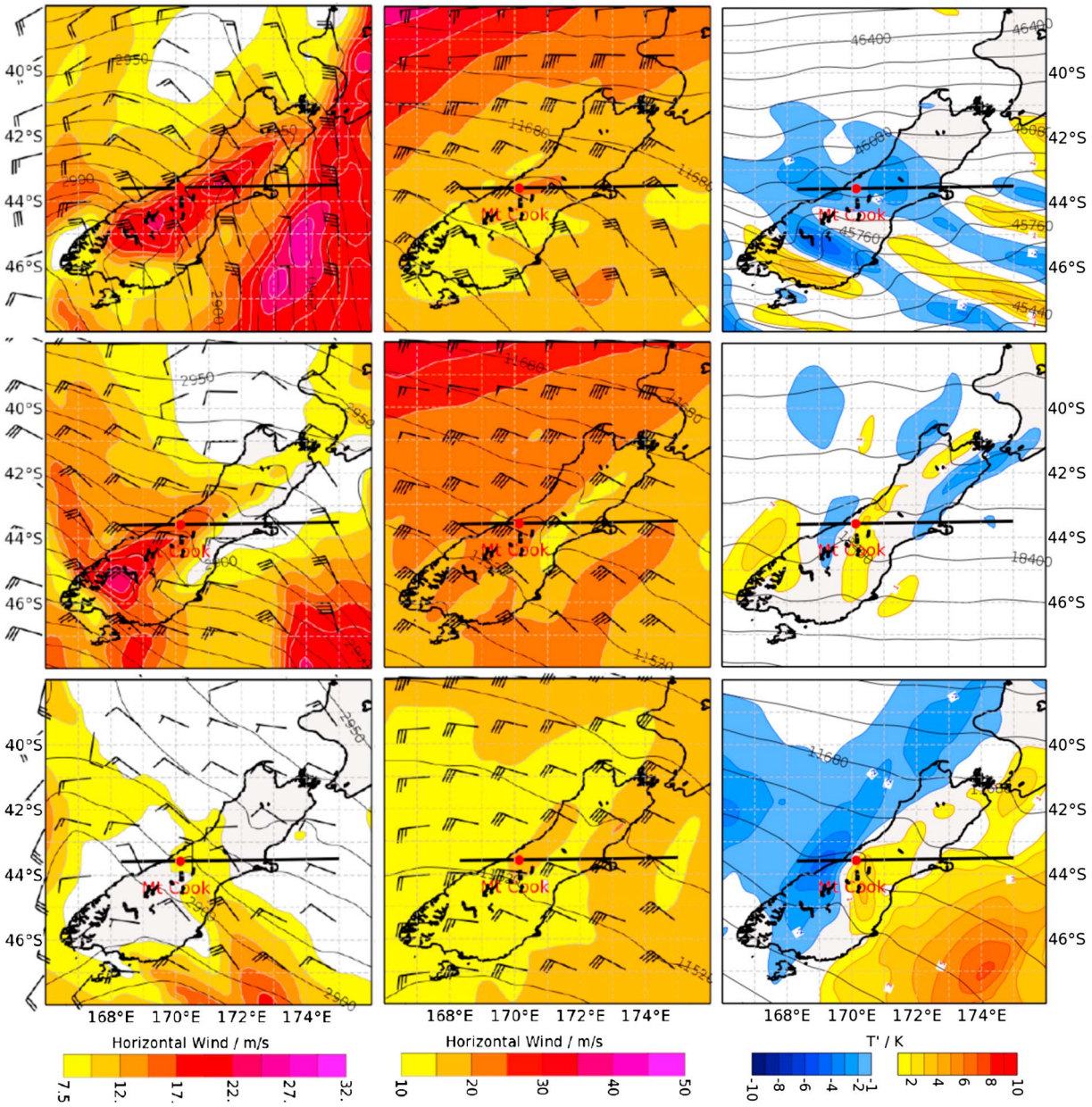

Figure 2. ECMWF 700- and 200-hPa winds (left and middle columns) at 06 and 18 UT on 12 July and 06 UT on 13 July (top to bottom). ECMWF T' at 200, 70, and 1 hPa (right, bottom to top) at 12 UT on 12 July. Wind barbs are 5 m/s. Magnitudes are shown with color bars at bottom. ECMWF = European Centre for Medium-Range Weather Forecasts.

components at higher altitudes (see the T' fields in the ECMWF reanalysis at 70 and 1 hPa in the top and middle panels at right in Figure 2). These increases in U and V below 30 km are expected to have allowed continued MW increases in λ_z and amplitudes to at least 30 km, except between ~17 and 25 km, where amplitudes may have been constrained by more uniform zonal winds.

The radiosonde u, v, and T profiles also exhibit apparent MW perturbations about the mean profiles throughout this interval, in a number of cases at scales, altitudes, and times that appear to correlate with changing mean winds at these and lower altitudes. At the earlier times accompanying strong cross-mountain flow, the MWs had λ_z ~ 2–5 km that appear to have increased in amplitude with altitude to ~17 km but decreased above to ~25 km. The latter suggests potential dissipation accompanying superposed large-amplitude MWs at these altitudes.

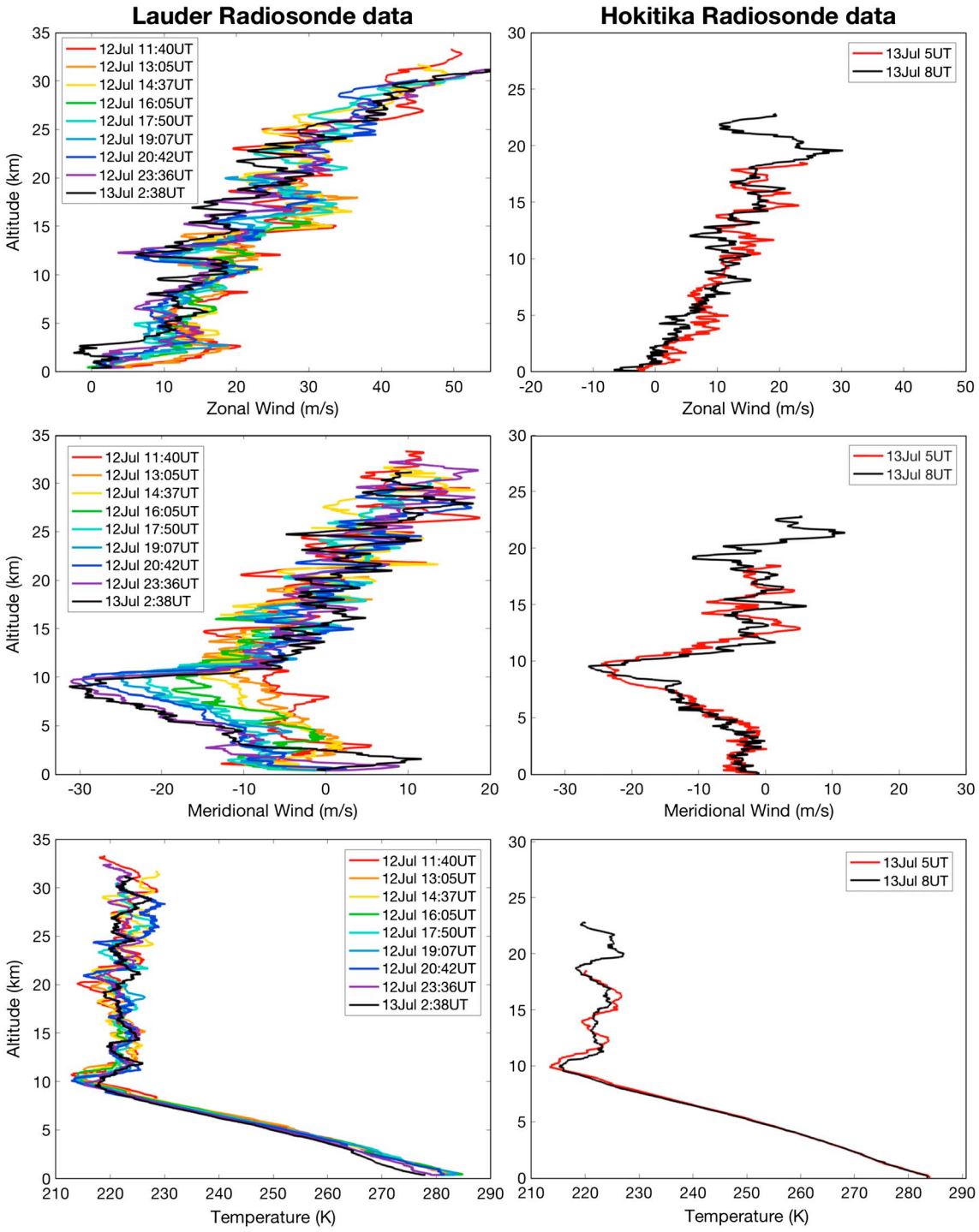

Figure 3. Lauder (left column) and Hokitika (right column) radiosonde zonal and meridional winds and temperatures (top to bottom) on 12 and 13 July (see legends for times).

At later times extending into the RF22 flight, apparent MW amplitudes decreased strongly with time throughout the lower stratosphere. Only at altitudes of ~10–17 km were there clear and persistent MW features in the u (z) and T (z) profiles having λ_z ~ 4 km. This value is consistent with λ_z estimated from equation (4) with U ~ 13 m/s and N ~ 0.01 s^{-1} at these altitudes. Importantly, both u (z) and T (z) profiles also reveal significant MW amplitude reductions at these altitudes accompanying significantly weakened forcing by ~20 UT on 12 July and continuing thereafter.

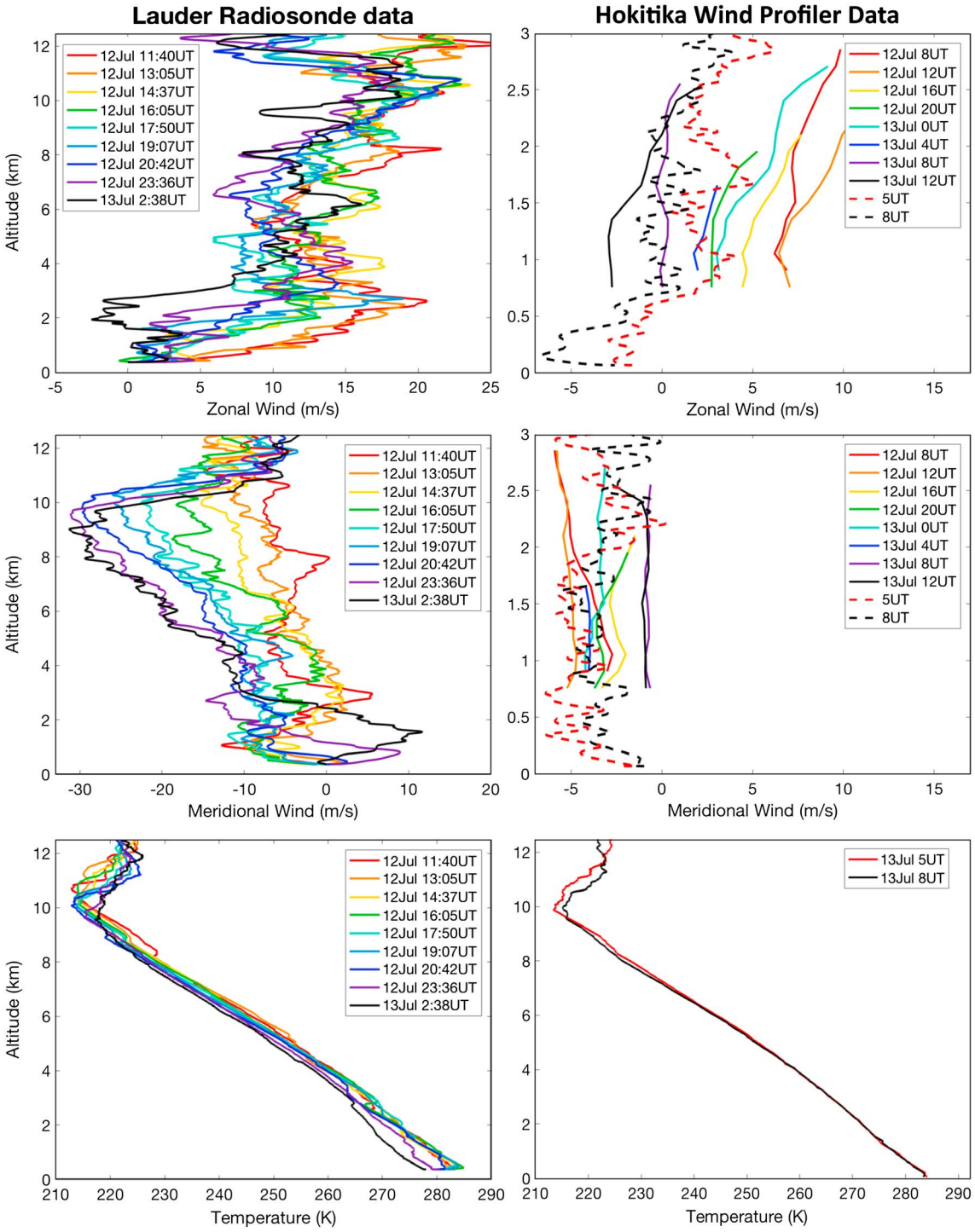

Figure 4. As in Figure 3 up to 12 km. Also shown at top and middle right are Hokitika wind profiler (solid lines) zonal and meridional winds below 3 km.

From equations (4) and (9), we see that $c_{gz} \sim U\lambda_z/\lambda_x \sim U^2/\lambda_x$ for hydostatic MWs propagating zonally. Hence, the MWs that will persist the longest at any altitude will have small ω_i, λ_z/λ_x, and U. For given U, MWs having larger ω_i (or λ_z/λ_x) will escape to higher altitudes more quickly. This likely accounts for the persistence of $\lambda_z \sim 4$ km MWs in the lower stratosphere having similar vertical phase structures and amplitudes over Lauder and Hokitika, implying primary contributions at small λ_x at the latest times (see the similar stratospheric profiles at late times in Figures 3 and 4).

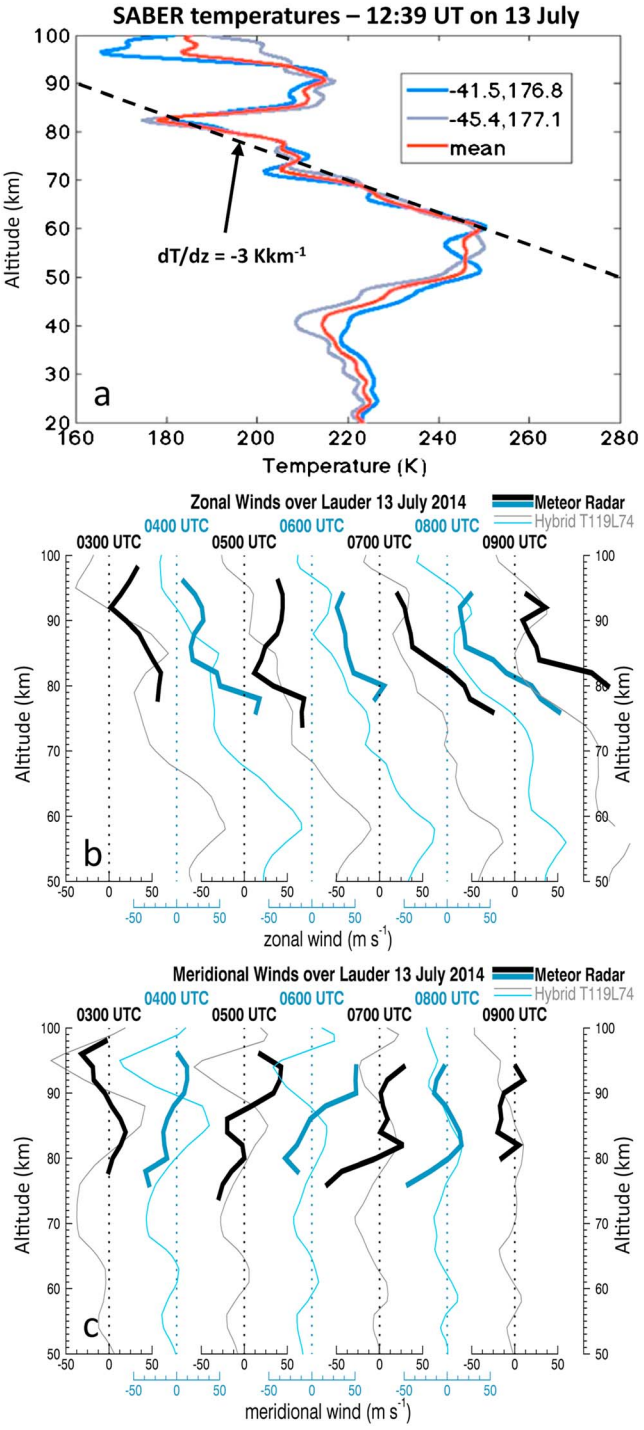

Figure 5. Nearest SABER temperature profiles at 41.5 and 45.4°S and their average centered near ~12:39 UT on 13 July (a). NAVGEM reanalysis zonal and meridional winds from 03 to 09 UT on 13 July (b and c). Thick lines in wind profiles are hourly means from the Kingston meteor radar. SABER = Sounding of the Atmosphere using Broadband Emission Radiometry; NAVGEM = NAVy Global Environment Model.

3.4. SABER, Meteor Radar, and NAVGEM *u*, *v*, and *T* Profiles

Limb *T* profiles obtained by SABER aboard the Thermosphere, Ionosphere, Mesosphere Energetics Dynamics satellite centered at ~45.4 and 41.5°S along an ascending orbit slightly east of the NZ SI during RF22 are shown at the top in Figure 5a (see Bossert et al., 2015, for further details). The profiles are somewhat similar, with the differences potentially reflecting variations in the large-scale MW responses in the lee of the Southern Alps at ~40 km and above where MW amplitudes became large (see Figures 8–12 below). The SABER *T* profiles also reveal d*T*/d*z* approaching the adiabatic lapse rate at altitudes of ~70–72 and ~78–82 km. The upper altitudes are those at which strong MW overturning was implied by the GV sodium lidar observations discussed in section 6. SABER *T* profiles thus provided both the large-scale context and some evidence of the local MW dynamics occurring during RF22.

Zonal and meridional winds measured by the meteor radar at Kingston, Tasmania, and obtained from the NAVGEM T119L74 reanalysis (Eckermann et al., 2018) from 03 to 09 UT on 13 July centered on Lauder are shown in Figures 5b and 5c. The differences between the radar and reanalysis winds above ~80 km likely reflect the 23° of longitude and 2° of latitude separation between the two sites, as well as the inference of a large semidiurnal tide at these latitudes on 13 July measured by the meteor radar and implied by NAVGEM reanalysis. At lower altitudes, NAVGEM indicates an expected zonal wind maximum of U~130 m/s centered slightly below 60 km spanning the 03–09 UT interval that agrees closely with that in the ECMWF analysis shown by Bossert et al. (2015).

Despite differences between the Kingston meteor radar and NAVGEM reanalysis winds at specific times, both data sets also suggest approach to a critical level near 90 km for MWs having largely zonal alignments. The consequence of a critical level would have been strong overturning and dissipation of large-amplitude MWs where increasing u' approached or exceeded decreasing U. Na lidar measurements discussed in section 6 were consistent with this expectation.

4. Flight-Level MW Characterization and Evolution

4.1. Flight-Level Measurements and Correlations

In situ measurements of u', v', w', p', and θ' at ~10.7 km along MC2 occurred on Leg 4 of FF9 and FF10 centered at ~19:00 and 23:45 UT on 12 July (see Figures 6a–6e at bottom and top, respectively, in each panel); also, see Bramberger et al. (2017) for more details of the Falcon flight-level data. These flight legs were nearly parallel to flight-level winds and nearly normal to the MW phases at flight altitudes, based on ECMWF wind and T' fields and radiosonde winds at 200 hPa at these times (e.g., Figure 2, middle and right columns, and Figure 4, top and middle left). Hence, measured λ_h were very nearly the true values on these Falcon flight legs.

The ~200-km Falcon flight legs exhibited peak u', v', and w' of ~10, 8, and 3 m/s, respectively, with the larger u', v', p', and θ' occurring at λ_h ~ 20–100 km or larger primarily over and downstream of Mount Cook. Significant perturbations were also seen at smaller scales, λ_h ~ 5–15 km, especially in w' and θ', and at intermediate scales at smaller amplitudes in all fields. Importantly, it was the intermediate to larger λ_h

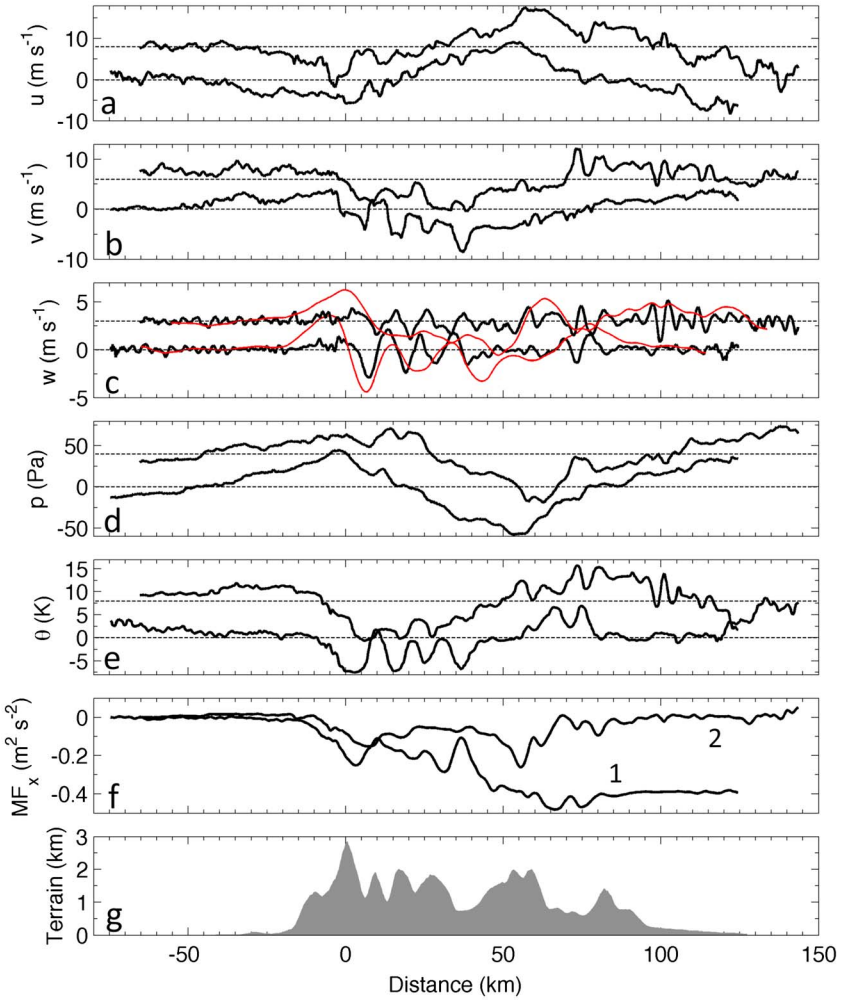

Figure 6. Flight-level *u*, *v*, *w*, *p*, θ', and cumulative $<u'w'>$ (a–f) for FF9 and FF10 (lower and upper lines in each panel). MC2 terrain is shown in (g); red lines in (c) show a 10-km running mean amplified by 7. FF = Falcon flight; MF = momentum flux.

(~20–150 km) that accounted for the major vertical fluxes of horizontal momentum (per unit mass), $<u_h'w'>$, along the flight legs.

Cumulative $<u_h'w'>$ (i.e., the integrated $u_h'w'$ beginning at the furthest upstream end of each flight leg) are shown for FF9 and FF10 in Figure 6f (also, see the discussion of wavelet spectra below). The major contributions on FF9 (labeled *1*) spanned ~100 km over and downstream of the highest terrain, with the major contributions by the larger λ_h.

The large w' at λ_h ~ 10–12 km on FF9 were largely in quadrature with v' at these scales, hence a largely trapped (or ducted) lee wave response within the layer of large d*T*/d*z* (large N^2) at ~10–12 km seen in the Lauder radiosondes in Figures 3 and 4.

Both the larger λ_h $<u_h'w'>$ and the trapped MW responses over the terrain were much smaller on FF10, consistent with the decreasing *U* across the terrain throughout 12 July.

By comparison, the contributions of $\lambda_h < 10$ km to the cumulative $<u_h'w'>$ over and downstream of the major terrain were very small on FF9 and FF10. Finally, the very similar character (and phases) of the responses seen in FF9 and FF10 in situ measurements, at larger and smaller scales, provided further evidence that the dominant contributions to these two fields comprised MWs rather than responses to other potential GW sources at these times.

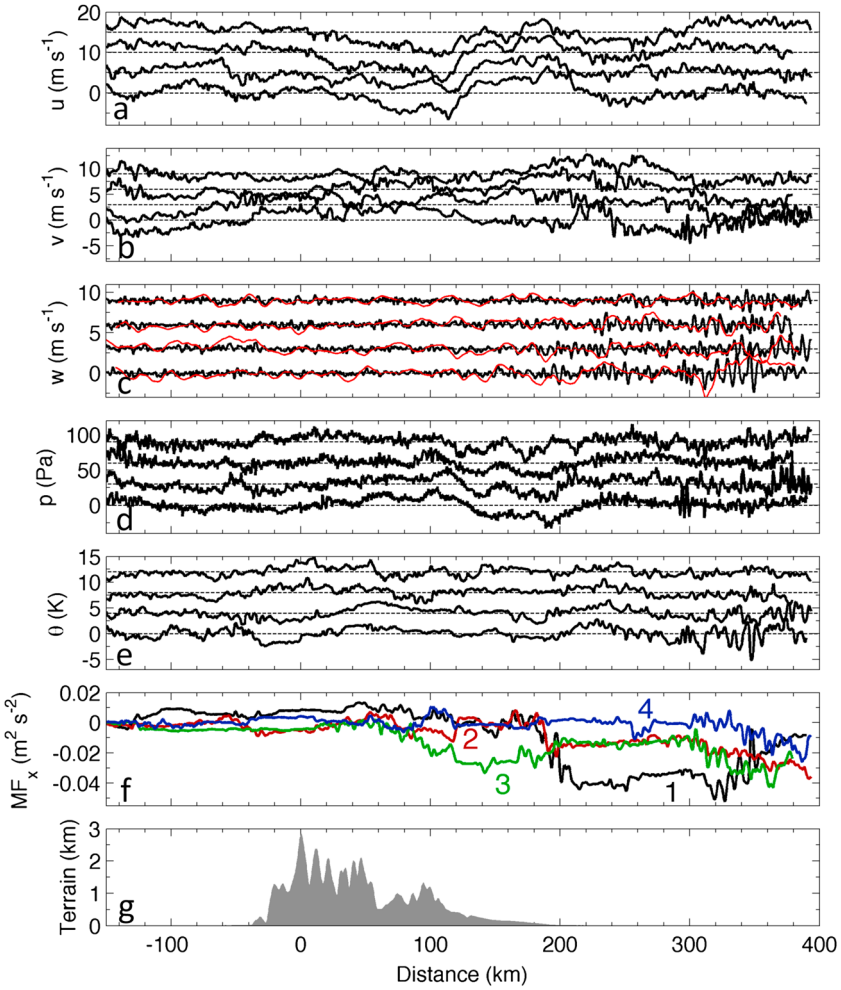

Figure 7. As in Figure 6 for the four legs of RF22 (bottom to top in each panel). (g) The MC1 terrain. Flight legs in (f) are labeled to distinguish the evolving cumulative $<u'w'>$. RF = Research Flight; MF = momentum flux.

Comparable in situ measurements at ~12 km by the GV during RF22 for the MC1 flight legs centered at ~6:34, 7:22, 8:08, and 8:52 UT on 13 July are shown in Figure 7. These data revealed similar or larger scales than those seen earlier by FF9 and FF10 but having smaller peak amplitudes and momentum fluxes accompanying the weakening flow over SI at lower altitudes. The flight-level winds and MW orientations appeared not to have changed appreciably from FF9 and FF10, and the somewhat larger λ_x seen by the GV along flight track MC1 were roughly consistent with those expected for the MWs measured by the Falcon along MC2 ~7–10 hr earlier. The ~550-km RF22 flight legs also revealed significant responses extending to λ_x ~ 100–300 km or larger, the smaller of which may have been the larger λ_h seen on FF9 and FF10. Importantly, however, the major upstream u' minimum, which was roughly over Mount Cook on FF9 and FF10, was nearly ~100 km downstream on the GV flight legs. This may have been a consequence either of decreasing cross-mountain flow extending into 13 July or MW phase differences due to different flight altitudes between FF9, FF10, and RF22 (see below).

As in the FF9 and FF10 in situ data, the largest contributions to negative $<u'w'>$ during RF22 occurred downstream of Mount Cook on the earlier MC1 flight legs, and the strong similarities of the four responses again supported the argument that these were largely MW fields arising from airflow over SI at earlier times.

Apart from the sensitivity of RF22 measurements to larger λ_x, due to its longer flight legs, a significant difference between the FF9–10 and RF22 flight-level responses was the character of the u field downstream from Mount Cook. Referring to Figures 6a and 7a, we note that u increased downstream in the FF9–10

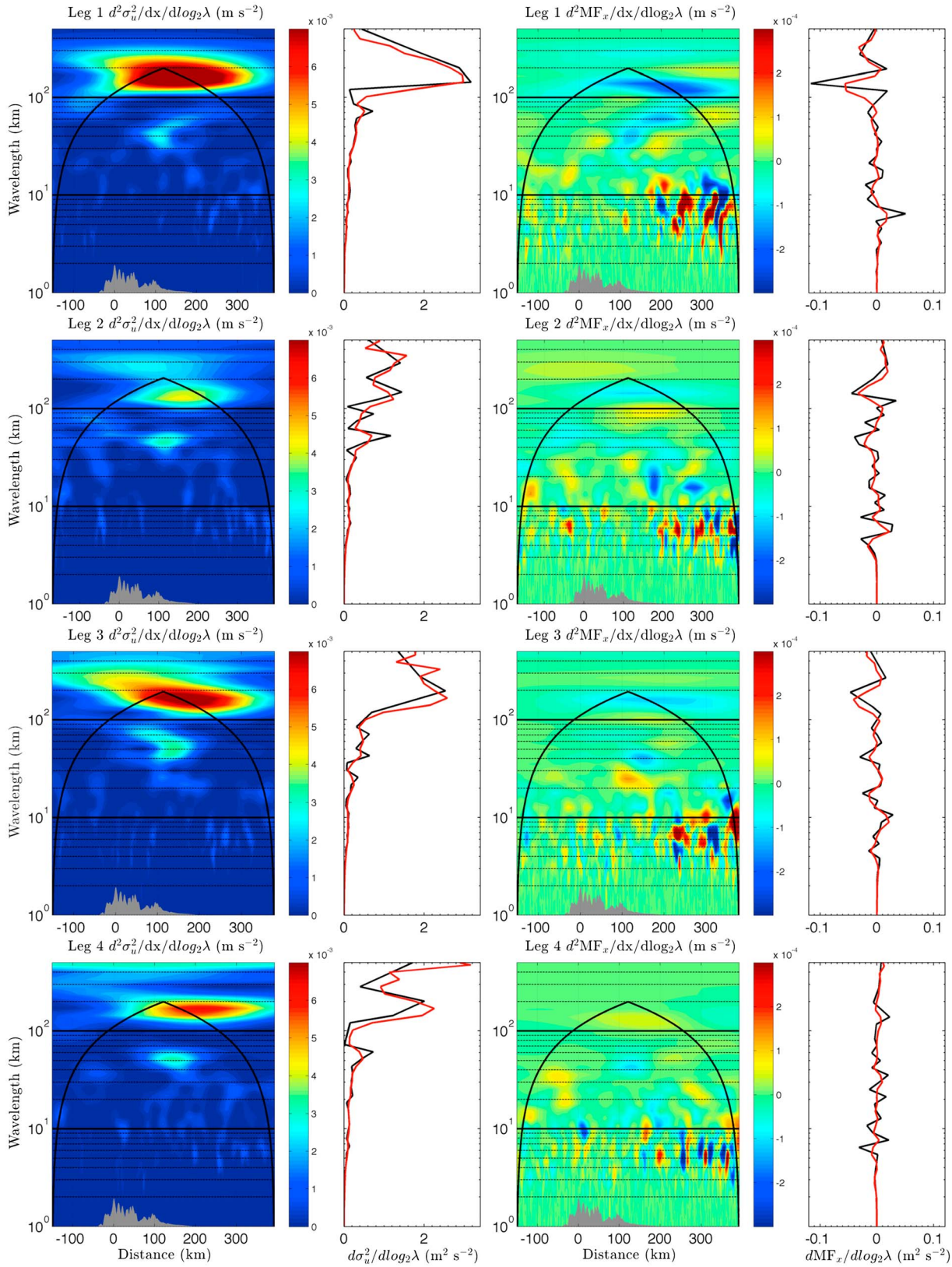

Figure 8. Wavelet $u'^2(k)$ spectra and $<u'w'>(k)$ cospectra as functions of position with respect to Mount Cook and horizontally integrated profiles (left and right columns) for RF22 Legs 1–4 (top to bottom rows). Red (black) lines are wavelet (Fourier) profiles smoothed to the same resolutions specified in the wavelet transform. RF = Research Flight; MF = momentum flux.

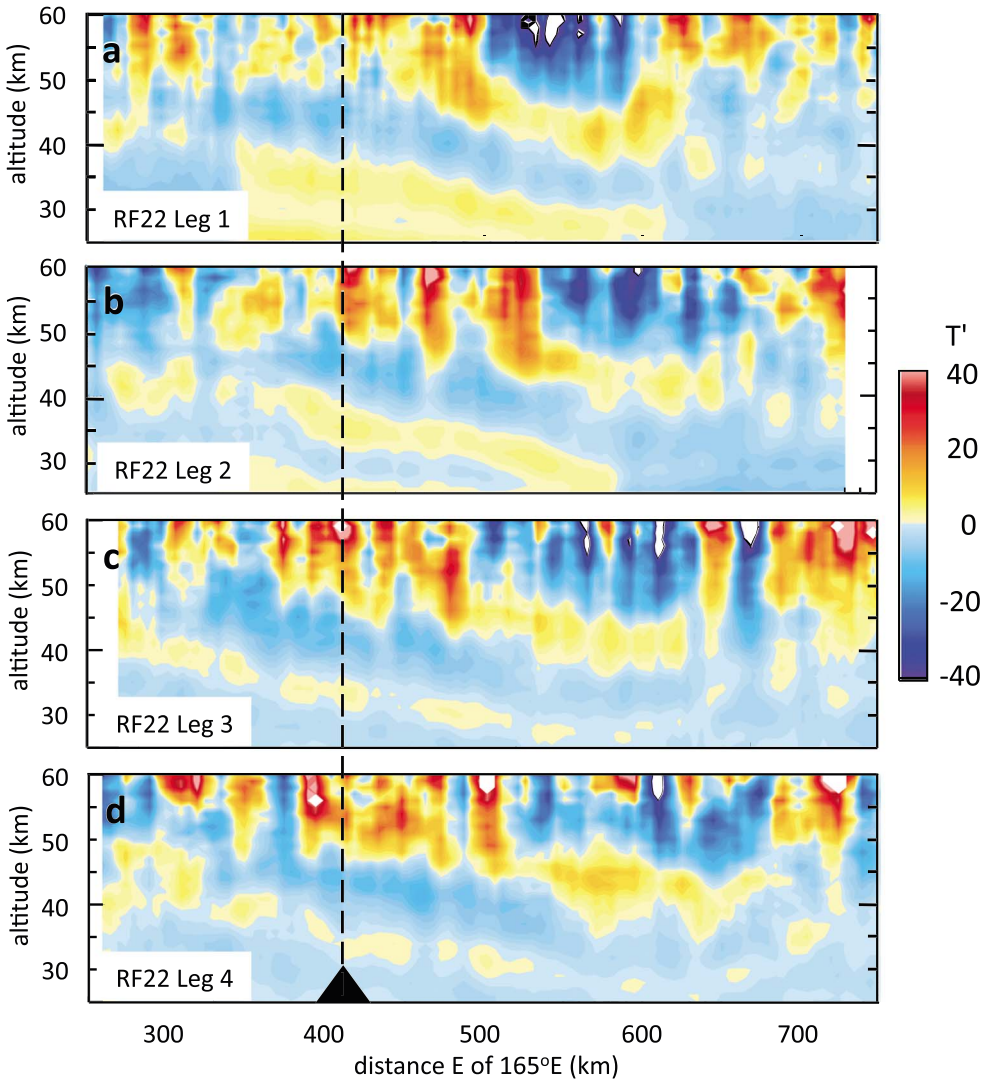

Figure 9. Rayleigh lidar $T'(x,z)$ averaged over 1 min (~12.5 km) and 3 km in altitude for the four legs of RF22 (a–d). The black triangle at bottom shows the location of Mount Cook.

measurements but decreased downstream in the RF22 measurements. While there was a significant interval between FF9 and FF10, and also between FF10 and RF22, the MW response appeared relatively stationary over the first interval and over the duration of RF22. Hence, changing forcing conditions appear unlikely to have accounted for the different behavior of u in the lee of Mount Cook, apart from decreasing MW amplitudes due to weakening forcing. These flights also differed by ~1.3 km in altitude, however, and in an environment with small U_h and large N, we expect a small $\lambda_z = 2\pi U_h/N$ from equation (4) for hydrostatic MWs. With U_h ~ 12–15 m/s and mean N ~ 0.02–0.04 s^{-1}, depending on altitude, we expect λ_z ~ 2–4 km, so a 1.3-km altitude difference suggests a significant MW phase variation, which may account for the u' behavior.

To examine the w' fluctuations accompanying the larger-scale MW responses seen in u' by FF9–10 and RF22, low-pass w' fields (10-km running mean, multiplied by 7) are shown with red lines in the w' panels in Figures 6 and 7. Those on Leg 1 revealed an approximately antiphase relation with $k < 0$, $m < 0$, small l, and $w'/u' < 0$ in equation (1), confirming the expected upward and largely westward phase tilt for vertically propagating MWs. As noted above, these MWs are expected to have been hydrostatic for λ_x ~ 20 km and larger at these altitudes. A nonzonal MW orientation, however, would imply a larger u_h' and smaller λ_h than seen in Figure 7. A closer inspection of the correlations in Figures 6 and 7 reveals evidence for various orientations at different λ_h and locations in all flights.

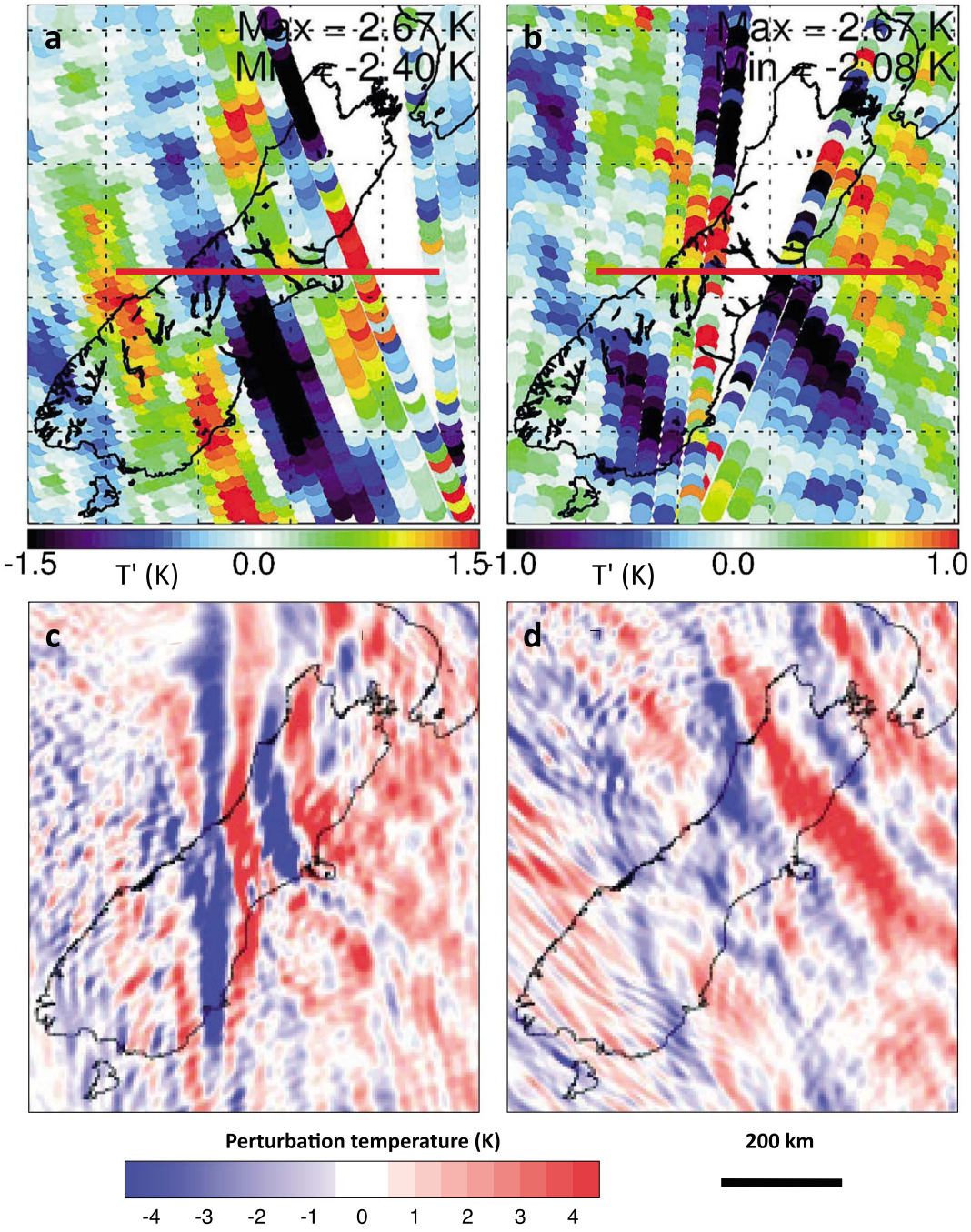

Figure 10. AIRS $T'(x,y)$ at 2 hPa (~43 km, a and b) on 13 July. Left and right images in (a) are at 01:41 and 03:19 UT on ascending passes; left and right images in (b) are at 12:48 and 14:27 UT on descending passes. Lower images are UM predictions at 02 and 14 UT (c and d) on 13 July. AIRS = Atmospheric Infrared Sounder; RF = Research Flight; UM = Unified Model.

Turning to the p' fluctuations shown in Figures 6d and 7d, we see p' and u' to have been strongly anticorrelated at MW λ_x ~ 100–300 km extending throughout each flight leg. This is expected for westward propagating MWs with $\omega_i = -kU$, which yields $p' = -\rho_0 U u_h'$ from equation (2). Similar correlations were also seen at MW λ_x ~ 80–100 km over the orography in Figure 6 and at λ_x ~ 30–100 km extending to ~200 km east in Figure 7 and were again consistent with upward propagation and energy fluxes.

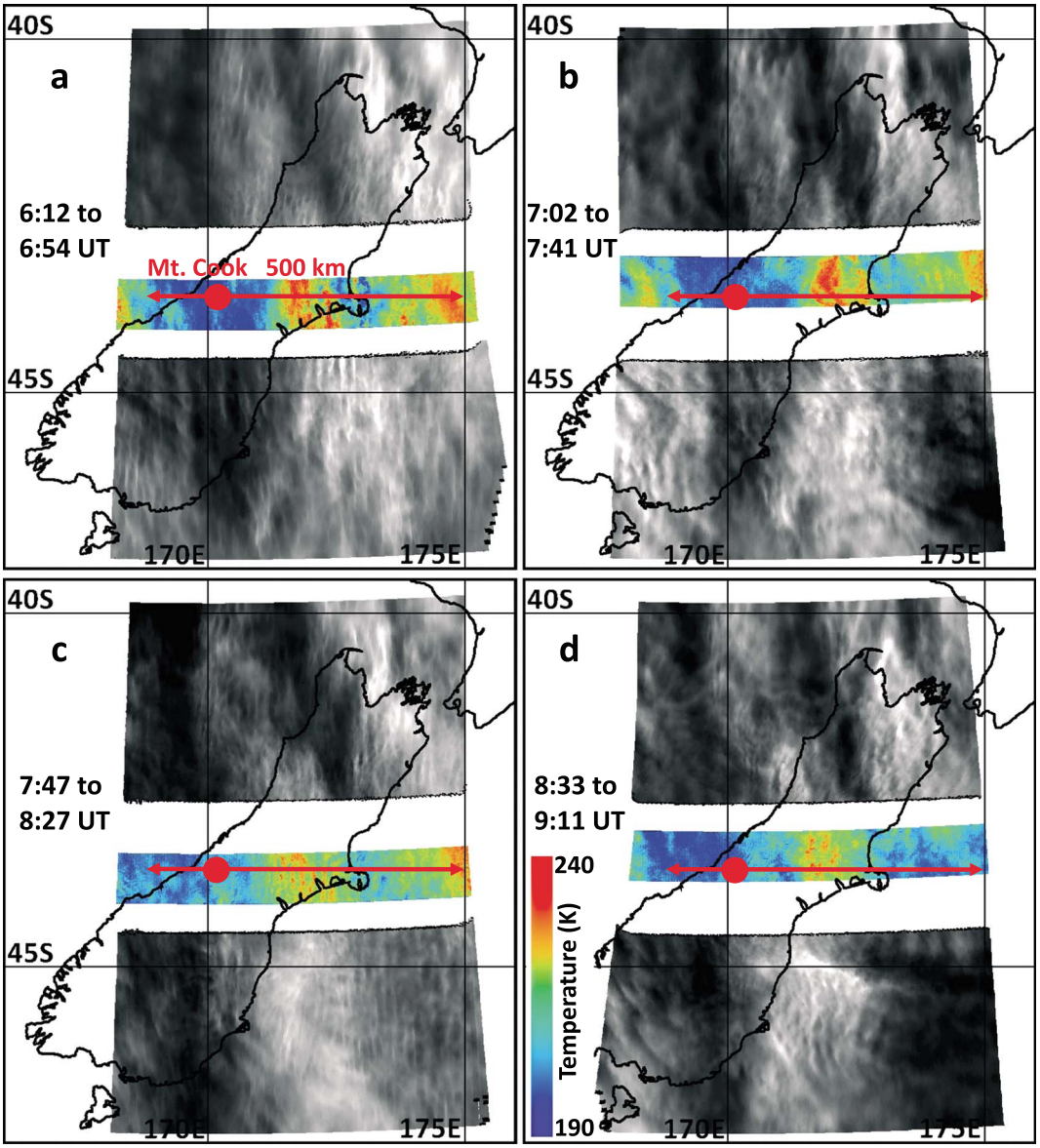

Figure 11. GV AMTM and IR camera composite imaging along Legs 1–4 (a–d). Red arrows show a distance of 500 km along each flight leg; the red dots show Mount Cook. The temperature scale is shown at lower left in (d). GV = Gulfstream V; IR = infrared.

At smaller scales, for example, λ_x ~ 10–20 km over the orography in Figure 6, u' and w' were more nearly in quadrature with p', indicating that smaller-scale MWs more easily experienced partial reflection and/or trapping near the altitude of elevated dT/dz and $N^2(z)$ and variable mean winds above the tropopause (see Figure 3). This was because penetration of a region having variable $N^2(z)$ and mean winds was more efficient for GWs having larger λ_h/λ_z for fixed λ_z (e.g., Fritts et al., 2018). The energy densities and fluxes implied by these correlations are discussed in greater detail in section 4.1.

The θ' fluctuations during RF22 are shown in Figure 7e. These reveal apparent responses to vertically propagating MWs at larger scales and to trapped lee waves at smaller scales that exhibited various correlations among and θ', u', and w'. We expect θ' to have been in approximate quadrature with u' and w' for vertically propagating GWs. We also expect θ' to have been in approximate quadrature with w' but more nearly in phase or antiphase with u' for trapped lee waves (see equation (3)) that readily arise in environments having variable structure in U (z) and $N^2(z)$, such as seen by R. B. Smith et al. (2008) in the Terrain-induced Rotor

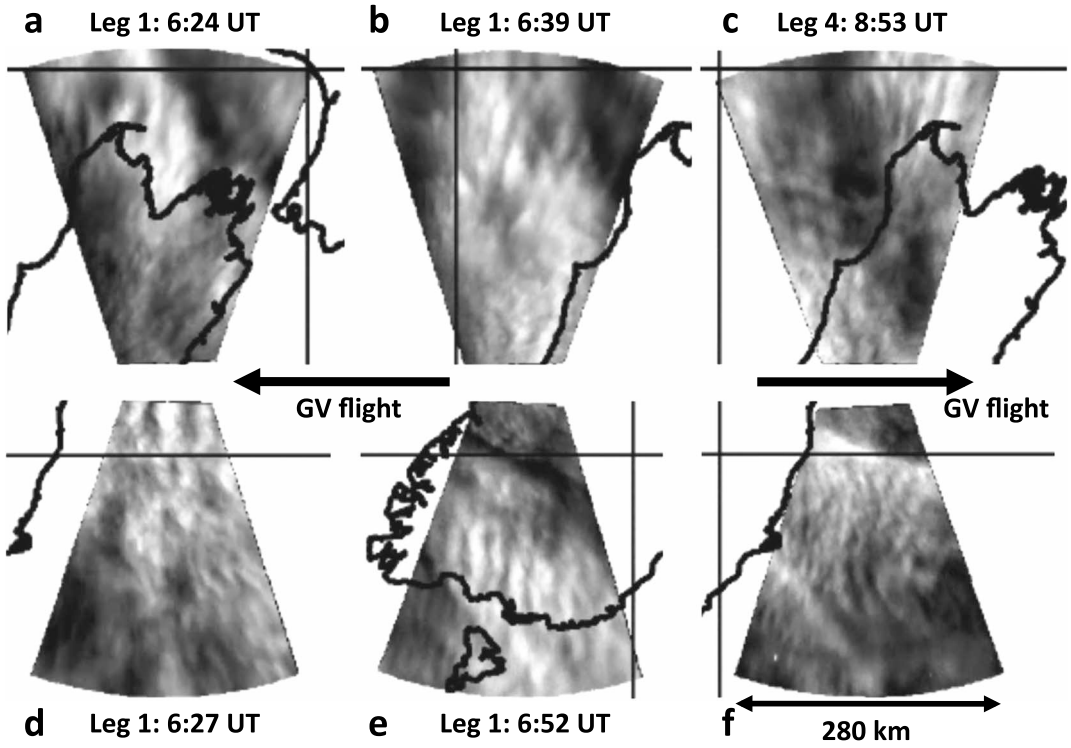

Figure 12. Wing camera images at four times on Leg 1 (a, b, d, and e) and at one time on Leg 4 (c and f). Images a–c are viewing north, and images d–f are viewing south.

EXperiment and in numerical simulations of multiscale flows by Fritts et al. (2013) and Fritts, Smith, et al. (2016). Specifically, the lowest two θ' plots exhibited clear maxima ~230 km eastward of Mount Cook somewhat downstream (eastward) of eastward u' maxima and w' minima, as expected for a westward propagating MW.

Evidence of trapped lee waves at λ_x ~ 6–8 km is provided by θ' maxima upstream of (leading) w' maxima by ~$\pi/2$ where both quantities were large (see these data between 300 and 400 km downstream during the first two flight legs). Correlations are clear in these cases because the GV was at 12 km throughout RF22, at which upstream soundings revealed an enhanced N^2 at these times (see Figures 3 and 4, bottom right), hence larger θ' for given u' and w'. Correlations of θ' with u' and w' are less pronounced during the third and fourth flight legs due to significantly decreased MW forcing prior to RF22 (see Figure 3, top row).

Finally, cumulative MW $<u'w'>$ on RF22 began on Leg 1 at ~10% of that seen by FF9 on 12 July and decreased to nearly 0 by Leg 4, due to cessation of MW forcing prior to this flight.

4.2. Flight-Level MW Energy and Momentum Flux Wavelet Spectra on 13 July

We now employ Morlet wavelet analyses to examine the evolutions of MW u' variance, $\sigma_u{}^2$, and zonal MFs per unit mass, $<u'w'>$, for the RF22 flight legs, following R. B. Smith et al. (2016), and assuming primarily zonal MW propagation for convenience. These wavelet spectra were computed in order to identify the dominant λ_x and locations of major contributions. These, and their integrations along the RF22 flight tracks, are shown in Figure 8.

The $\sigma_u{}^2$ spectra and flight leg integrations in the left column in Figure 8 reveal that the dominant variances at these times occurred at λ_x ~ 100–300 km, with significantly smaller contributions (~10%) at λ_x ~ 40–80 km and very little at $\lambda_x < 40$ km. These spectra also exhibit significant variability in the u' variances from leg to leg that are also seen in the flight-level u' in Figure 7a. The most probable explanation for this variability at flight level is the highly variable wind field over Lauder spanning the ~6–12 hr prior to RF22. Specifically, $U(z)$ at MW forcing altitudes of ~1–3 km was seen at top right in Figure 4 to decrease from ~15 m/s to ~0

from ~19 UT on 12 July to 2:38 UT on 13 July. These decreases resulted in generally decreasing MW forcing and $T'(z)$ seen to occur late on 12 July and the apparent absence of MW T' in the two $T(z)$ profiles early on 13 July at bottom in Figure 4. However, note the variable cross-mountain flow seen in Figure 4 within the overall decrease in $U(z)$ at these times discussed above.

Finally, we note that the much weaker u' variances at smaller λ_x during RF22 relative to those inferred from the flight-level data for FF9 and FF10 in Figure 6 were due to the much larger MW c_{gz} at smaller λ_x; see equation (9) for a uniform MW λ_z for hydrostatic MWs. Thus, the MWs having the largest λ_x were the last to be seen at flight altitudes as the forcing diminished.

In contrast, the $<u'w'>$ spectra and flight leg integrations at the right column in Figure 8 show that the dominant local contributions at any one time most often accompanied GW motions having λ_x ~ 10–60 km. Of these, those having λ_x ~ 10 km or less were almost certainly trapped lee waves, given the oscillatory character of their $<u'w'>$ on short zonal scales. Those at intermediate λ_x ~ 20–80 km were also often somewhat oscillatory but at larger zonal scales more commensurate with their λ_x. The oscillatory character of these MW responses was likely a consequence of MW reflections approaching the $U(z)$ maximum of ~130 m/s at ~55–60 km expected for $\lambda_x \sim 2\pi U/N \sim 40$ km, at which $\omega_i = kU$ approached N_0, yielding $c_{gz} \sim 0$ and MW reflection; see equation (9). Indeed, only at the larger scales, λ_x ~ 40–200 km (and larger on Leg 1 and largely absent on Leg 4), were there regions of systematic negative $<u'w'>$ extending over significant downstream distances (due in part to their longer wavelengths), as seen in Figure 7f discussed above.

5. Stratospheric MWs and Possible Other GWs

5.1. GV Rayleigh Lidar $T'(x,z)$ Cross Sections

Temperature perturbations measured with the GV Rayleigh lidar at altitudes from 25 to 60 km along the four flight legs performed on RF22 are shown in Figure 9. These fields reveal larger-scale GWs having λ_x ~ 150–200 km and ~250–300 km that appear to have been relatively stationary in space, but decreasing in time, that were largely consistent with the decreasing forcing discussed above. The larger of these extended from ~200–300 km downstream to ~100 km or more upstream of Mount Cook. The stationary phase and its close correspondence with the underlying terrain are persuasive evidence that this is a large-scale MW.

This MW exhibited a λ_z that increased from ~10 km at ~35 km to ~30 km or larger at ~50–55 km. The latter is consistent with that expected for a hydrostatic MW from equation (4) at ~60 km, for example, $\lambda_z = 2\pi U/N_0 \sim 40$ km due to its increasing U with altitude. The MW T' likewise increased strongly with altitude, varying from a few K or smaller below 35 km to ~20 K or larger at 60 km.

The λ_x ~ 150–200 km response was more prevalent above ~40 km on Legs 1 and 2, began ~100 km in the lee of Mount Cook, and decreased more rapidly with time. Specifically, it appeared to counter the positive T' phase of the λ_x ~ 250–300 km MW beyond ~150–200 km in the lee of Mount Cook, and it yielded very significant T' enhancements above ~50 km at ~50 and 200 km in the lee of Mount Cook. Thereafter, it appeared to be replaced above ~50 km by the longer MW, which had a smaller c_{gz}, hence a longer residence time at all altitudes. These responses were also consistent with a MW interpretation at these scales (and with the flight-level observations in Figures 6 and 7), given their different c_{gz} and the weakening forcing and variable propagation environment at lower altitudes. Both of these longer MWs appear to have achieved a T' ~ 20 K at 60 km but at difference times.

Seen at smaller λ_x ~ 20–80 km above ~45 km are additional GWs that had either much larger λ_z or evanescent behavior. We also interpret these GWs as MWs because of consistency of their λ_x with flight-level observations, their occurrence primarily in the lee of the Southern Alps (Figures 6–8), and their largely negative $<u'w'>$ at these locations (see right column of Figure 8). As noted above, the strong zonal winds seen in the NAVGEM reanalysis (Figure 5) at 55–60 km caused MWs with λ_x ~ 40 km and less to become evanescent at these altitudes and reflect, accounting for their vertical phase structures seen in Figure 9. MW λ_x greater than about 40 km would have continued to propagate vertically but become strongly nonhydrostatic at the U maximum, thus achieving finite but larger λ_z than hydrostatic MWs. These MW amplitudes were T' ~ 10–20 K or larger, and those that propagated to higher altitudes increase in amplitude into the mesosphere.

Referring to equations (5) and (6ab), we infer a hydrostatic MW u_h' ~ 40 m/s for T' = 20 K and a MW amplitude a ~ 0.3, well below a ~ 1 required for MW breaking. The larger λ_z for nonhydrostatic MWs at λ_x ~ 40–80 km imply that they had smaller a for comparable T'. Hence, both the hydrostatic and nonhydrostatic MWs seen in Figure 9 would have increased in amplitude as ~$e^{z/2H}$ (apart from diminution due to horizontal dispersion) as they propagated to higher altitudes. As they did so, however, U decreased rapidly with increasing altitude above 60 km, such that a ~ $|u'|/U$ increased rapidly and approached or exceeded a ~ 1 somewhat above ~70 km.

5.2. AIRS $T'(x,y)$

Stratospheric nadir radiances from 15 μm CO_2 emissions measured by the Atmospheric Infrared Sounder (AIRS) channels were used in near-real time during DEEPWAVE to image GWs at altitudes otherwise accessible only by the GV Rayleigh lidar (Fritts, Smith, et al., 2016). Figures 10a and 10b show inferred temperature perturbations from a ~2-hPa (~43 km) AIRS radiance channel. Each panel shows successive overpass swaths separated by ~98 min. Ascending overpass data (Figure 10a) were obtained at ~01:41 and 03:19 UT (right and left swaths); descending data (Figure 10b) were obtained at ~12:48 and 14:27 UT (right and left swaths). The most relevant swaths were those ~3 hr before and ~4 hr after RF22 Legs 1 and 4, respectively. The later (Figure 10a) ascending $T'(x,y)$ field exhibits large-scale MW perturbations aligned ~NNW-SSE that were negative over and downstream of Mount Cook and positive ~150 km to the east and west (see the RF22 flight track shown in red); thus, they were distinctly different than along the major orography as seen at lower altitudes. Importantly, these T' variations along the flight track (red lines) agreed closely with those seen by the GV Rayleigh lidar on all flight legs extending to ~6 hr later. However, the AIRS T' ~ 2–3 K maxima and minima were substantially smaller than the lidar T' ~ 8–10 K at ~43 km, due to the significant averaging depths of the nadir radiance kernel function compared to the MW λ_z ~ 15 km at this altitude.

The latter AIRS composite image suggests significant variability in the MW field in time and that large-scale MWs persisted to much later times in the middle-to-upper stratosphere due to their small c_{gz}, despite cessation of forcing near 00 UT on 13 July.

6. Mesospheric MWs

As noted previously, MW responses in the mesosphere during RF22 were large and extended from λ_x ~ 30–300 km. Clear links between large-scale MWs in the stratosphere and mesosphere during RF22 enabled by largely linear propagation over ~70 km in altitude due to relatively weak forcing were noted previously by Fritts, Smith, et al. (2016). Bossert et al. (2017) showed that the smaller λ_x in the mesosphere were primarily secondary GWs that were most apparent in the warm phases of the larger-scale MW discussed above. Here we examine in greater detail the coherence of MWs from the stratosphere into the mesosphere, the evidence for MW breaking, the evolution of the MW field with altitude, and the associated MW momentum fluxes.

6.1. GV AMTM and IR Camera Observations

The horizontal structures of the MW (and other GW) field observed in the OH airglow at ~87 km along and across each of the RF22 flight legs are shown in Figure 11. Images for each flight leg are a composite from the central cross-track pixel rows of the GV overhead Advanced Mesosphere Temperature Mapper (AMTM) and infrared (IR) *wing* cameras imaging the OH layer to the north and south. Together, these comprise a cross-track field of view of ~900 km and define the apparent scales and orientations of multiple MWs, secondary GWs (e.g., Bossert et al., 2015), and potentially other GWs at multiple sites, scales, and amplitudes spanning the ~4-hr duration of RF22.

Dominant OH brightness and T' variations accompanied the larger-scale MWs that were seen to vary slowly over the duration of RF22. The largest scales were λ_x ~ 200 and ~300 km to the north and south, respectively, on each leg that were fairly stationary in time, implying an anticlockwise rotation of the MW phase from west to east. The airglow features thus had phase alignments varying from nearly N-S at the western edge of these measurements to roughly NNW-SSE that were roughly consistent with that seen in the AIRS image at top right in Figure 10. These structures did exhibit temporal variability, however, suggesting either modulation of the dominant MW amplitude or a superposition of MWs at different scales

that varied between successive flight legs. The approximate stationarity of these structures, and their apparent upward extension from MW features at the same scales seen at lower altitudes, is compelling evidence that these variations were due to the MW field itself, rather than to GWs from other sources. Also seen were intermediate and smaller scales of λ_h ~ 15–150 km that were much more variable along each leg and between successive legs.

Examples of the larger-scale spatial and temporal variability include the following:

1. weaker modulations of brightness in the NW and NE quadrants on Legs 1 and 3,
2. weaker responses in T' north of the flight track on Leg 3, and
3. weaker modulations of brightness in the SW and SE quadrants on Legs 1 and 2.

Smaller-scale structures were highly variable, for reasons described, in part, by Bossert et al. (2015). In those cases, which focused on the AMTM overhead imaging, the dominant small-scale variances were correlated to a high degree with regions where the larger-scale MWs yielded a maximum T'. However, there were multiple additional sites that exhibited similar, apparently transient, intermediate- and smaller-scale GWs and potential instabilities that may or may not have had MW origins. Those at intermediate scales, λ_h ~ 40–150 km, were seen in all phases of the λ_h ~ 200–300 km MW. In contrast, those at small apparent scales, λ_h ~ 15–40 km, appear to have occurred primarily in the brighter (warmer) phase of the λ_h ~ 200–300 km MW. Importantly, true λ_h differed from *apparent* λ_h for GWs having nonzero phase propagation with only single pixel row sampling.

The clearest examples of intermediate-scale λ_h ~ 40–150 km variations are seen in the slowly varying brightness between successive flight legs to the north from ~170–175°E. The roughly stationary character of these features, and the agreement of their scales with those seen at lower altitudes, suggest that these brightness variations were also due to MWs that propagated from below and penetrated the strong zonal jet peaking at ~55–60 km noted above.

To aid in the interpretation of the smaller-scale GWs having λ_h ~ 15–40 km, we show in Figure 12 airglow brightness images from the side-viewing cameras at four times on Leg 1 and both north and south views at one time on Leg 4. Whereas the images in Figure 12 capture the true spatial structures of the various GWs in the field of view, the composite images in Figure 11 overestimate or underestimate λ_x (effectively a spatial Doppler shift) if GW phase propagation is along or opposite to the GV flight direction, respectively. This yields an apparent $\lambda_x = \lambda_{xo}\ (U_{GV} + c)/U_{GV}$ and an implied $c = U_{GV}\ (\lambda_x/\lambda_{xo} - 1)$ inferred by comparing the true and composite images.

The composite and true images in Figures 11 and 12 reveal the following λ_x ~ 15–40 km features:

1. GWs at multiple sites along Leg 1 exhibited approximately zonal alignments (~N-S phases), steepening, and roughly linear phases (also see the supporting information Movie S1).
2. GWs seen at small λ_x at multiple sites exhibited strong shifting to smaller λ_x, implying large eastward phase speeds, especially on Legs 1 and 3.
3. Multiple GWs during Leg 3 exhibited similar evolutions and motions as on Leg 1.
4. Similar GW scales, structures, and evolutions occurred during Legs 2 and 4 but in these cases having more variable phase motions.

AMTM and airglow camera images described above reveal a dynamically active and highly variable environment spanning apparent GW scales of λ_x ~ 15–300 km at ~87 km. The dominant time scale at larger spatial scales appears to be roughly the separation between flight Legs 1 and 3 (and Legs 2 and 4), ~94 min, given the strong modulations of λ_x ~ 200-km u' variances at flight level (Figure 8) and airglow brightness on alternating legs. These slow, large-scale λ_x ~ 200 km variations appear to have imposed variability in the character, especially the rapid eastward phase motions, of the λ_x ~ 15–40 km GWs seen on Legs 1 and 3. The faster of these yielded λ_x ~ 0.6–0.7λ_{x0} and implied c ~ 60–80 m/s for U_{GV} ~ 210 m/s, hence eastward propagation at ~87 km at $c - U$ ~ 30–40 m/s with respect to U ~ 30–40 m/s at these times (see Figure 5b). These GWs cannot have arisen in the troposphere or lower stratosphere, due to the strong zonal jet at ~55 km. Nor could they easily have propagated from sources far upstream, given their λ_z ~ 10 km or larger implied by their observed c. Hence, they were most likely secondary GWs generated by MW breaking at lower altitudes in the mesosphere (e.g., Bossert et al., 2015).

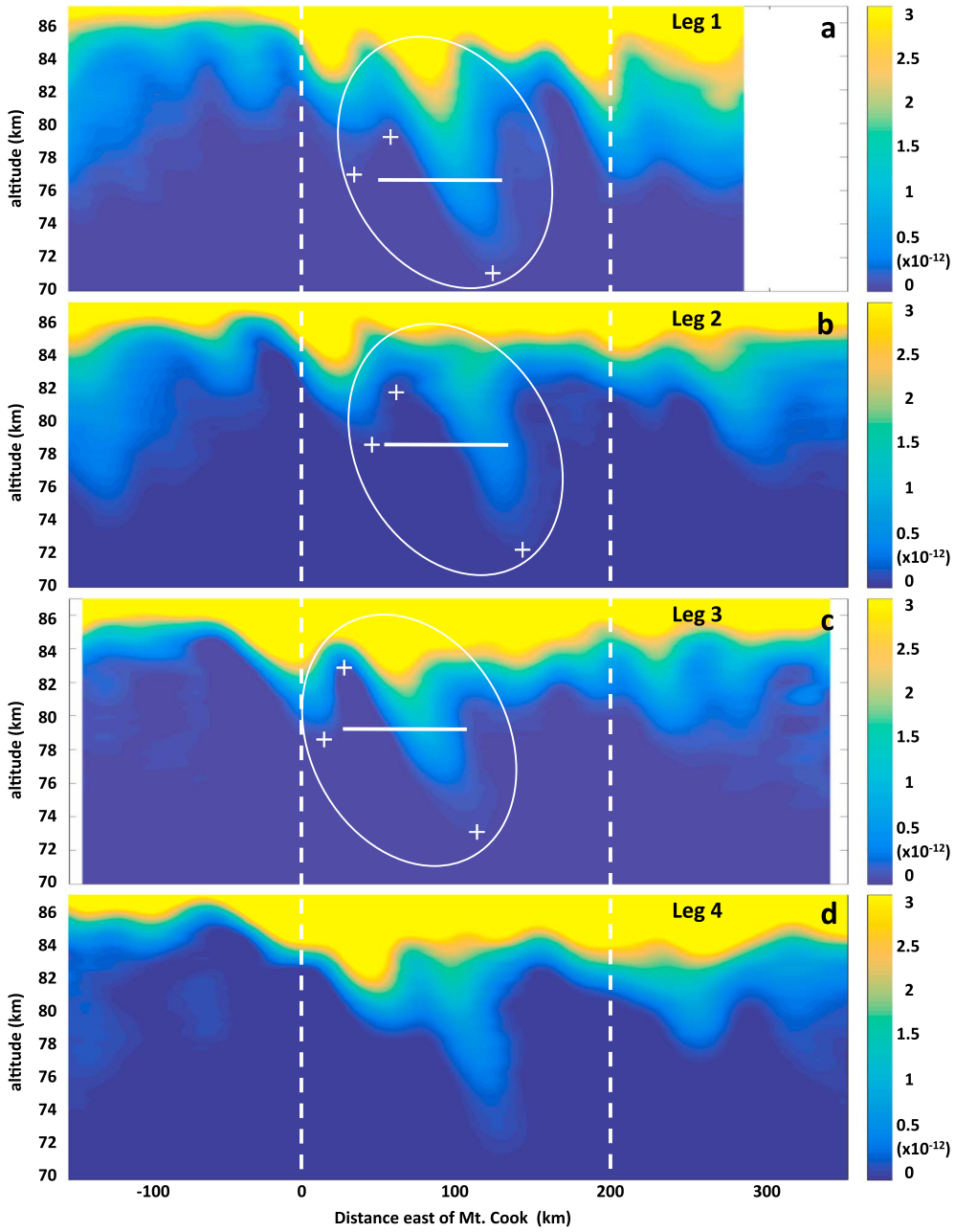

Figure 13. Estimated Na mixing ratios, R_{Na} (x,z), at the bottom side of the Na layer for the four legs of RF22 (a–d). Note the peak-to-peak excursions exceeding ~10 km on each leg. White ovals and horizontal lines show the cases and central altitudes of the MW features used to compute local $<u'w'>$ estimates. The +'s show the ζ' extrema estimated from R_{Na}. Central times for the four flight legs were ~6:33, 7:20, 8:07, and 8:52 UT. RF = Research Flight.

6.2. GV Na Lidar Mixing Ratios

Na density measurements by the GV Na lidar during RF22 extended from ~70 to above 100 km. These data were used to provide estimates of the mean and perturbation Na mixing ratios, $R_{Na0}(z)$ and $R_{Na}'(x,z)$ along each flight leg (see Figure 13), in order to explore MW dynamics in the mesosphere with the highest possible resolution, ~3.6 km along track and 1.8 km in altitude. Laser locking was sporadic on Legs 2 and 3, however; hence a low-pass filter having a passband of 100 s (~24 km) and a stop band of 50 s (~12 km) retained MWs at λ_x ~ 30 km and larger (see Bossert et al., 2018, for further details). These data enabled identification of MW λ_x, vertical and horizontal parcel displacements, $\zeta'(x,z)$, and regions of overturning within the MW field.

Our method was as follows. We assumed $dR_{Na}/dt \sim 0$, implying that R_{Na} is a good tracer of MW $\zeta'(x,z)$. This was justified by detailed Na chemistry modeling of MW modulations of the Na layer, where R_{Na} was predicted to be elevated by at most ~20% due to adiabatic warming accompanying downward ζ' of ~5–6 km over three MW cycles (also see Bossert et al., 2018). Hence, to be conservative, the deepest downward MW ζ' were estimated from measured R_{Na} 50% higher than the lowest contour. We also assumed that $d\theta/dt = 0$, given the short MW intrinsic period, $T_{MW} = 2\pi/\omega_i \sim 20$ min, and $T_0(z,t)$, $H(z,t)$, $N_0(z,t)$, $U_0(z,t)$, and other parameters estimated from SABER $T(z)$ and NAVGEM reanalysis fields. Together, these enabled estimates of MW (1) $T'(x,z)$ and λ_x from $R_{Na}'(x,z)$; (2) λ_z from λ_x, $N_0(z,t)$, and $U_0(z,t)$; (3) u' and w' from these quantities using equations (1) and (3); and (4) peak $<u'w'>$ for several specific MW features discussed in section 6.3 below (see Bossert et al., 2018, for a more complete description of the Na chemistry modeling).

$R_{Na}(x,z)$ cross sections in Figure 13 reveal MW responses at $\lambda_x \sim 30$–300 km, with peak-to-peak ζ' ~ 10–11 km at the smaller (and steeper) λ_x on each leg (see the maximum ζ' excursions shown with white +'s in Figures 13a–13c). On all legs, the largest upward ζ' at the higher altitudes occurred over and upstream of Mount Cook and were consistent with the weaker airglow brightness that correlated well with negative T' in these MWs (see the correlations along each leg near the flight tracks in Figure 11). The longer MWs made major contributions to upward ζ' in this region because they extended further upstream at lower and higher altitudes than MWs having smaller λ_x due to the shallower propagation angles and dispersion for larger λ_x (see Figures 6–9 and 11).

The largest apparent downward ζ' occurred at ~100–150 km downstream of Mount Cook. These ζ' were larger than any observed in the mesosphere by any ground-based Na lidar to date of which we are aware. They also implied very large u' and w', and among the largest local estimates of GW $<u'w'>$ in the mesosphere inferred from other observations to date (see below).

Also seen in Figure 13 is evidence of initial MW overturning and incipient breaking ($dR_{Na}/dz < 0$) at the downstream edges of the deeper descending R_{Na}' maxima and of potential prior mixing upstream on all legs (see the less coherent features also having $dR_{Na}/dz < 0$ at several sites). These features are only seen clearly above ~75 km and suggest that the MWs required further amplitude growth from $T' \sim 20$ K at 60 km (see discussion of Figure 9) to achieve overturning amplitudes. For reference, conservative propagation and continuing exponential growth would yield a further increase by ~3 times (and overturning amplitudes, $T' > 50$ K) above ~75 km.

A summary of the more significant results of this section includes the following:

1. Deep tongues of elevated R_{Na} extended up to ~5–6 km below their equilibrium altitudes, with chemical enhancements of as much as 20% extending the lower extrema.
2. True peak-to-peak ζ' were ~10 km or larger on each leg and as large as ~9 km between adjacent MW minima and maxima (especially Legs 1–3).
3. Steeper phase slopes occurred at smaller λ_x (Leg 1 at upper left, Leg 3 at upper right).
4. Regions of $dR_{Na}/dz < 0$ indicated deep overturning in MW field at ~75–84 km.
5. Less coherent and distinct R_{Na} variations at ~75–84 km suggested 3-D instabilities and mixing at multiple sites where MW amplitudes were strongly reduced.

6.3. GV Na Lidar MW Momentum Fluxes

The $R_{Na}(x,z)$ fields discussed above imply very large MW amplitudes and momentum fluxes peaking at altitudes where instability dynamics driven by increasing amplitudes and decreasing $U(z)$ began to occur. We expect these dynamics to have constrained MW amplitudes to $a \sim 1$ or somewhat above, hence strongly decreasing ζ', T', and u' below a MW critical level near 90 km where $U = 0$ (assuming largely zonal propagation). The $R_{Na}(x,z)$ fields in Figure 13 reveal this to have been the case.

We now employ the R_{Na} fields in Figure 13 to provide estimates of momentum fluxes (per unit mass), $<u'w'>$, where R_{Na} variations are well defined. We first estimate the peak-to-peak vertical displacements over a MW λ_x at the lowest altitudes where the largest excursions are easily defined. Because there are multiple superposed MWs, the maximum upward and downward ζ' are not generally symmetric; hence, upward excursions were defined by the upper +'s in Figures 13a–13c, and downward excursions were defined by the average altitudes of the two lower excursions (lower two +'s) in Figures 13a–13c. The peak-to-peak depths (central altitudes) for

the three MW structures in the white ovals on Legs 1–3 were 5.1 (76.6), 6.1 (78.5), and 6.9 (79.4) km, respectively. Those on Leg 4 exhibit superpositions that preclude clear identification of a single large-amplitude MW. Importantly, in the three cases considered, the smallest dR_{Na}/dz at the central were very near 0, implying an amplitude $a = |u'|/U = 1$ to a very good approximation.

The SABER T (z) at top in Figure 5 implies a mean gradient $dT_0/dz \sim -3$ K/km (see dashed line fit) and a mean $N_0 = 0.0175$ s^{-1} for $T_0 = 200$ K. Thus, $\zeta' = 1$ km implies $T' = -6.5$ K for conservative displacements, and equation (5) yields $|u_h'| = (g/N_0)|T'/T_0| = 17.65$ m/s for hydrostatic MWs. The inferred MW displacements then imply $u' \sim 46$, 54, and 61 m/s on Legs 1–3, respectively. Inspection of the NAVGEM U at these times suggests interpolated $U \sim 64$, 48, and 45 m/s at the respective central altitudes of the ζ' estimates. The inferred $u' \sim 48$ m/s for the MW on Leg 1 is less than the NAVGEM U, in contradiction to that implied by $a = 1$ for this MW. In contrast, the inferred $u' \sim 54$ and 61 m/s for the MWs on Legs 2 and 3 are larger than the NAVGEM U at these altitudes and times, also in contradiction to those implied by $a = 1$. We note, however, that the Kingston meteor radar zonal winds (measured ~1,800 km to the west) are likewise larger than those from NAVGEM. Hence, we will use R_{Na} and U inferred from the Na lidar measurements, with $a = |u'|/U = 1$, as the best estimates of $\lambda_z \sim 2\pi U/N_0$ and $w' \sim -\lambda_z u'/\lambda_x$.

We estimate $\lambda_x \sim 57$, 75, and 63 km for the three cases from the descending phases of high R_{Na} and λ_z and w' using $U = u'$. The latter yield $\lambda_z \sim 17$, 20, and 22 km and $w' \sim 14$, 15, and 22 m/s. These estimates yield peak momentum flux estimates of $<u'w'> = -(2\pi g^2/N_0^3)(T'/T)^2(U/\lambda_x)$ of ~300, 390, and 650 m^2/s^2 for the three cases, assuming hydrostatic MWs. The corresponding wavelength ratios are $\lambda_z/\lambda_x \sim 0.30$, 0.27, and 0.35. These reveal that the highlighted MWs were nonhydrostatic and thus had larger nonhydrostatic λ_{znh} and $<u'w'>_{nh}$ by factors of $(1 - \lambda_z^2/\lambda_x^2)^{-1/2}$. For the MW events discussed here, these factors are 1.05, 1.04, and 1.07, yielding more accurate $<u'w'>_{nh} \sim 310$, 410, and 690 m^2/s^2.

Given the above relations for $<u'w'>$ and $<u'w'>_{nh}$, their uncertainties are dictated by those in N_0, $T'/T \sim \zeta'$ in R_{Na} (z), λ_x, and U. SABER T (z) in Figure 5 suggest a roughly uniform dT_0/dz from 50 to 90 km with independent potential T_0 and dT_0/dz uncertainties of ~5 and 10%, implying an uncertainty in N_0^3 of ~20%. Uncertainties in R_{Na} (z) and inferred ζ' and T'/T are estimated to each be ~10%, hence ~20% for $(T'/T)^2$. Those in λ_x are estimated at ~10%, while those in U are judged to also have a 10% uncertainty, given the R_{Na} fields and gradients, and high-resolution modeling showing strong GW breaking and amplitude constraints at $a = |u'|/U \sim 1$ (Fritts et al., 2009a, 2009b). These independent uncertainty estimates lead to a cumulative uncertainty of ~60% in the estimates of $<u'w'>$.

While the uncertainty estimates are large, the $<u'w'>$ estimates are very large. Even assuming the minimum estimates, these imply very large momentum flux divergence and local flow accelerations accompanying MW dissipation that must have occurred below a MW critical level anticipated by NAVGEM and the Kingston meteor radar to have occured near 90 km. Further discussion of these results, their comparisons with others, and their implications is provided in section 8.

7. Met Office UM Simulations

As noted above, the Falcon and GV flights on 12 and 13 July spanned an interval of rapidly decreasing MW forcing. This resulted in significant reductions in flight-level MW amplitudes and vertical momentum fluxes but more delayed and sustained responses at larger MW λ_x and higher altitudes due to their slower vertical propagation and larger propagation depths (see Figures 6–9).

To aid the interpretation of these observations, the UM (Version 10.4), was employed for five simulations having horizontal resolutions of 2, 4, 8, 16, and 32 km. The simulations were initialized at 12 UT on 12 July 2014, prior to the interval of strong mean wind accelerations and decelerations preceding the FF9, FF10, and RF22 flights (see Figure 4).

UM simulations over SI employed a rotated latitude/longitude grid nested within a global UM forecast initialized with the Met Office operational analysis, 118 levels up to 78 km, and a damping layer above 58.5 km. The 2-km resolution simulation employed 1,100 × 1,100 grid points centered on the SI. The range of resolutions was specifically intended to explore the impact of model resolution on the resolved MW amplitudes and momentum fluxes with increasing altitude. Additional UM details are provided by Vosper et al. (2016).

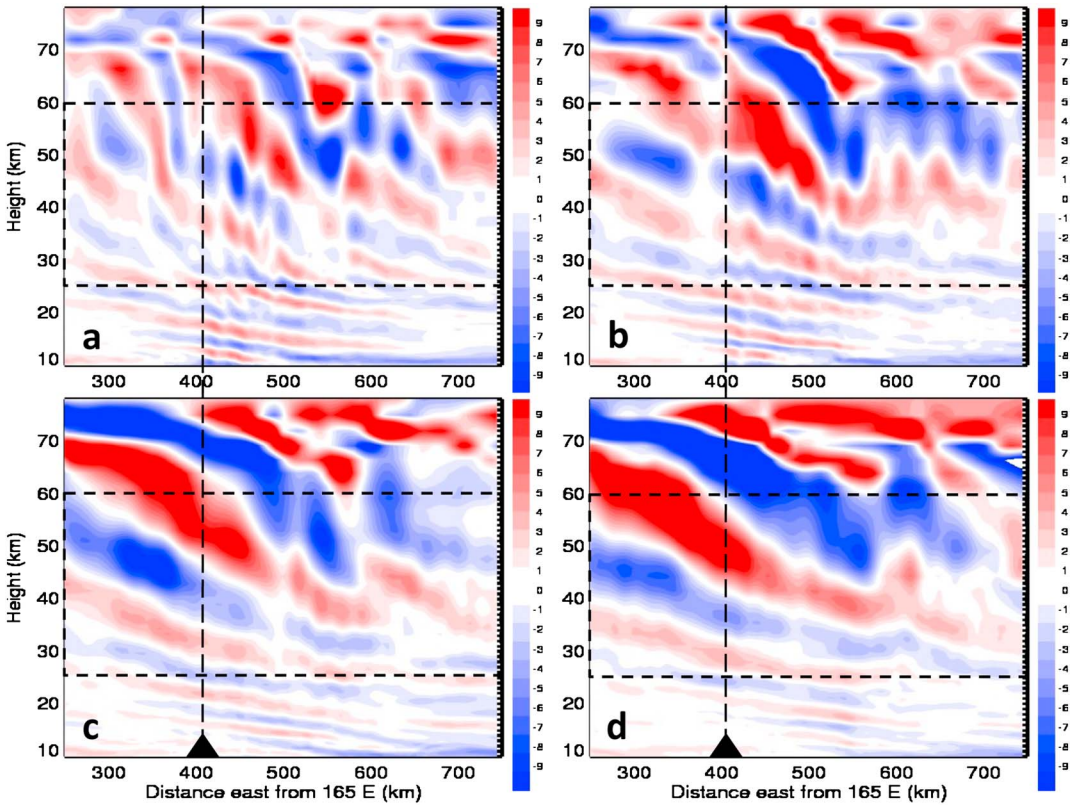

Figure 14. Met Office UM T' fields along flight track MC1 at 00, 03, 06, and 09 UT (a–d). (c and d) At the approximate times of the Rayleigh and Na lidar measurements on Legs 3 and 4 shown in Figures 9 and 13. Horizontal dashed lines show the upper and lower altitudes of the Rayleigh lidar measurements in Figure 9. Vertical dashed lines show the location of Mount Cook for comparison with the AMTM, IR camera, and lidar fields shown in Figures 8, 11, and 13. Also note the different color scales here compared to those in Figure 9 (smaller by 4 times). UM = Unified Model; IR = infrared.

UM outputs for RF22 were used to generate along-track vertical (x,z) and horizontal (x,y) cross sections of T' and vertical profiles and wavenumber spectra of momentum fluxes for comparisons with GV airborne lidar and imager observations and to aid the interpretation of the RF22 observations. Specific outputs examined below include the following:

1. $T'(x,z)$ cross sections along flight track MC1 on 13 July, computed by removing domain mean $T_0(z)$;
2. $T'(x,y)$ cross sections in the stratosphere, computed by subtracting T (x,y) from an equivalent simulation without NZ terrain;
3. $\rho <u'w'>$ (z) and $\rho <v'w'>$ (z) profiles from ~6 to 62 km averaged over the local UM domain and from 05 to 09 UT; the velocity perturbations are computed by removing fields from the *flat orography* run at each time; and
4. $\rho <u'w'>$ zonal wavenumber spectra computed from the hourly flux data in item (3) above; spectra are presented for all five simulations at 30 km and also for the 2-km resolution simulation at 40, 50, and 58 km.

7.1. UM $T'(x,z)$ Cross Sections

$T'(x,z)$ cross sections from the 2-km resolution UM simulation extending ~550 km along the MC1 flight track at altitudes from 10 to 78 km at 00, 03, 06, and 09 UT on 13 July are shown in Figure 14. The altitudes and horizontal extent within the dashed rectangle in each panel correspond to the altitudes shown for the GV Rayleigh lidar in Figure 9; the distance scales are the same in Figures 9 and 14 for easy reference. Note, however, that the lidar data correspond to only the two later cross sections in Figure 14.

The UM $T'(x,z)$ fields in Figure 14 exhibit variations of λ_z with altitude that reflect the varying U_h (z,t) and $N_0(z,t)$ for each component of the MW field in accordance with equation (4). For largely zonal alignments, λ_z ~ 5–10 km are implied from ~10–30 km up to ~03 UT on 13 July, and these scales are seen in the UM fields at these times and altitudes. From ~30 to 60 km, however, U increases from ~40 to ~130 m/s, enabling λ_z ~ 30 km or larger between ~40 and 70 km, and a local maximum λ_z ~ 40 km at the U (z) peak (see Figure 14 at 03–09 UT and equation (4)). λ_z in the UM decrease above ~60 km due to decreasing U (z), which implies a MW critical level near 90 km. MW amplitudes and λ_z above ~60 km are influenced by the UM damping layer beginning at 58.5 km, however, and thus likely depart increasingly from reality at higher altitudes. In contast, variations of λ_x with altitude and time are dictated by the terrain scales and $c_{gz} \sim \lambda_z/T_{MW} \sim U/T_{MW}$ for a MW period $T_{MW} \sim \lambda_x$; this supports the statement above that MWs with large λ_x require long times to reach high altitudes where small U imply small c_{gz} at lower altitudes.

The weakening cross-mountain flow and apparent cessation of MW forcing that began near 12 UT on 12 July (see Figure 4, top row) effectively decouples the MW response from the forcing prior to RF22. This accounts for the weakening of the larger λ_x (~300 km) MWs below ~30 km and the decreasing amplitudes of the smaller λ_x (~20–80 km) MWs throughout the model domain over the interval displayed in Figure 14. In contrast, the ~100–200 km MWs in the UM fields persist to later times. The ~300-km MW even increases in amplitude at higher altitudes over this interval due to its very small $c_{gz} = \omega_i/m = \lambda_z U/\lambda_x$ and hence long residence times at lower altitudes.

We now turn to a comparison of the UM MW $T'(x,z)$ cross sections within the dashed rectangles in Figure 14 with the GV Rayleigh lidar $T'(x,z)$ observations in Figure 9. Note that the GV Rayleigh lidar fields roughly span the final two times shown for the UM.

There are many similarities that suggest that the high-resolution UM has succeeded in capturing the major features of the observed event. Both the observations and the model exhibit MW responses from λ_x ~ 30–300 km, with the largest scales predominant below ~35 km, and the intermediate and smaller scales, λ_x ~ 30–200 km, becoming important above ~40 km. Approximate agreement is also seen in the phases of the observed ~300 km MW with those seen in the UM, and in the λ_x ~ 150–200 km at ~40 km and above downstream of Mount Cook beginning and after 03 UT (Figures 9 and 14b–14d). Finally, both observations and the UM results reveal a decrease in large- and intermediate-scale MW activity below ~45 km by ~09 UT but having large-scale responses that persist to much later times than the cessation of forcing near 00 UT on 13 July. These similarities indicate that the UM captured key aspects of the MW forcing and propagation at the full range of λ_x observed.

There are also differences, however, and these are seen primarily in the amplitudes and timing of the MW responses predicted by the UM relative to the Rayleigh lidar observations. While the overall character of the MW response, that is, the phase structures and locations of the various components, are realistic, the amplitudes in the UM are roughly half those in the observations at $\lambda_x > 100$ km throughout the common altitude range. As an example, the large-scale MW exhibiting a phase variation from warmer westward to colder eastward over Mount Cook has a maximum amplitude of T' ~ 8 K in the observed fields at ~35–40 km on Legs 1 and 2 at ~6:30–7:20 UT and of T' ~ 3–4 K at 03–09 UT in the UM. UM amplitudes are even smaller at $\lambda_x < 100$ km at ~50–60 km altitudes, where both UM and lidar MW amplitudes are better defined.

Another significant difference is the timing of the intermediate- and smaller-scale MWs, λ_x ~ 30–150 km, at altitudes of ~40 km and above. These MWs were seen in section 4.1 to be significant at flight level during FF9 centered at ~19 UT on 12 July but to diminish dramatically at flight level thereafter on FF10 and RF22. Given their sustained forcing prior to FF9 and their relatively large c_{gz}, they would easily have reached the upper stratosphere and mesosphere by 00 UT on 13 July. UM results are consistent with this expectation, exhibiting significant responses at these scales extending to ~60 km, above which the smaller scales are preferentially removed by the UM sponge layer above 58.5 km. These MWs are still significant in the UM T (x,z) field at 03 UT on 13 July (Figure 14b) but diminish significantly by 06 UT and almost entirely by 09 UT. In contrast, the Rayleigh lidar data reveal that the intermediate-scale MWs, λ_x ~ 80–150 km, decrease in amplitude very slowly over the duration of RF22, while the smaller scales, λ_x ~ 30–80 km, decrease very little.

There are several possible reasons for the above differences. In the case of the amplitude variations at lower altitudes, it is likely that there is significant numerical dissipation in the UM where λ_z and c_{gz} are very small, as is the case in the lower stratosphere and especially in the troposphere having even smaller U (z); see Figures 4 and 14. Specifically, numerical dissipation is a function of spatial resolution, and the UM results here at the highest spatial resolution may nevertheless allow significant dissipation where spatial scales are small (see section 7.4).

At higher altitudes, λ_z and c_{gz} are very large, and UM resolution is not an issue. The UM sponge layer beginning at 58.5 km is designed to damp all motions at higher altitudes independent of their spatial scales. This damping will act on all MWs occurring above 58.5 km, hence potentially reducing amplitudes of the smaller-scale MWs that reflect at these altitudes due to the large U (z). We consider it unlikely, however, that this damping would reduce reflected MW amplitudes appreciably at lower altitudes. Another possible mechanism accounting for smaller-scale features in the MW field at higher altitudes is nonlinearity of the large-scale MW, as seen to occur at higher altitudes in the 2-D simulation of the RF22 event by Heale et al. (2017). But the large-scale MWs in the UM simulation do not reach amplitudes sufficient to become nonlinear, and the smaller-scale MWs are seen at flight altitudes (see Figure 8). Thus, at present, the only viable explanation for cessation of smaller-scale MWs at higher altitudes prior to their disappearance in the Rayleigh lidar data appears to be limitations of the UM to accurately account for MW excitation and initial propagation where λ_z and c_{gz} are very small in the troposphere and lower stratosphere at earlier times.

7.2. UM $T'(x,y)$ Cross Sections

An additional evaluation of UM MW predictions is enabled by AIRS temperatures at 2 hPa (~43 km) in the stratosphere shown in Figures 10a and 10b. As noted above, each AIRS image is composed of two ascending or descending measurements separated by ~98 min, but only the second ascending image is useful here. UM $T'(x,y)$ cross sections at 02 and 14 UT between the successive AIRS measurements in each panel are shown in Figures 10c and 10d.

The eastern edge of the AIRS nadir $T'(x,y)$ image at 03:19 UT on 13 July (Figure 10a) was seen in section 5.1 to be in reasonable agreement with the Rayleigh lidar $T'(x, z = 43$ km) along RF22 Leg 1 at ~6:32 UT roughly 3 hr later. However, this AIRS image and the UM $T'(x,y)$ field 79 min earlier in Figure 10c do not agree in their dominant MW scales or their phase orientations. The explanation for these differences appears to be the long time required for the λ_x ~ 300 km MW to propagate from mountain top to 43 km. With $c_{gz} = \lambda_z^2/\lambda_x T_b$ and the vertical variations of λ_z and T_b, this time is ~15 hr after attainment of full forcing at mountain top, which is after 03 UT on 13 July, given the initiation of the UM simulation at 12 UT on 12 July. Hence, the UM $T'(x,y)$ field was necessarily dominated by MWs having smaller λ_x at this time.

The implications of UM and AIRS field comparisons in the stratosphere are several. Examples include the following:

1. The UM appears to capture the dominant MW scales and orientations seen in the stratosphere and the mesosphere, though with a delay arising from a UM initiation that was too late to describe the λ_x ~ 300 km MW responses in the stratosphere seen early on RF22.
2. Comparable AIRS and UM T' extrema in the stratosphere imply significant UM T' underestimates, given known AIRS underestimates due to deep weighting functions.
3. AIRS and UM fields suggest that the RF22 MW event duration in the stratosphere and mesosphere extended to significantly later times than the aircraft measurements.

7.3. UM $\rho <u'w'>$ (z) and $\rho <v'w'>$ (z) Profiles

Profiles of zonal and meridional momentum fluxes averaged over the UM domain from 06 to 09 UT on 13 July are shown in Figure 15a. The largely westward momentum fluxes are consistent with the dominant MW orientations observed in the stratosphere and mesosphere. Significant reductions in their magnitudes with altitude below ~9 km appear to reflect constraints on MW amplitudes by weak winds in the troposphere contributing to strongly decreasing MW activity at flight level spanning RF22 (see Figures 4, top row, and 7). Increasing U (z) up to ~15 km (Figure 3, top row) enabled MWs to propagate conservatively at these altitudes, above which more uniform U (z) between ~15 and 25 km again suppressed increasing MW amplitudes with

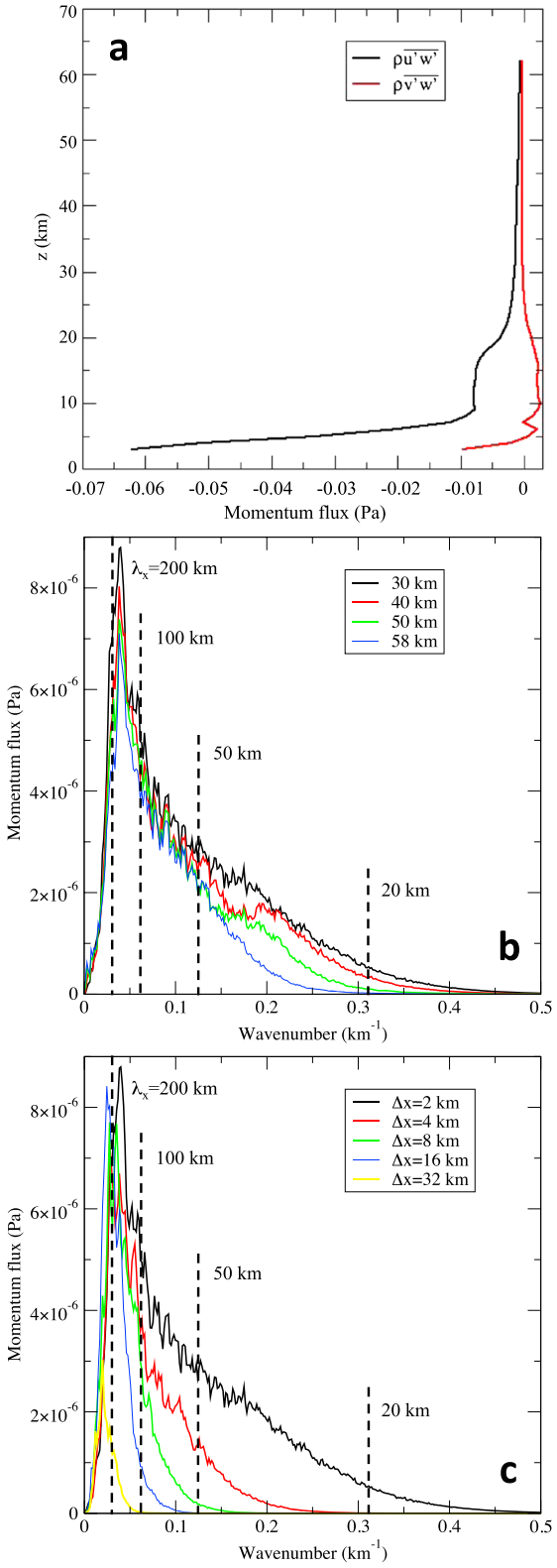

Figure 15. Met Office UM domain-integrated $\rho <u'w'>$ and $\rho <v'w'>$ (a), $\rho <u'w'>$ (k) spectra at 30, 40, 50, and 58 km (b), and $\rho <u'w'>$ (k) spectra at 30 km at horizontal resolutions of Δx = 2, 4, 8, 16, and 32 km (c; see legends in all panels). Vertical dashed lines in (b) and (c) show representative λ_x. UM = Unified Model.

altitude. Importantly, however, the strongly decreasing $\rho <u'w'>$ does not preclude significant MW responses at 60 km and above.

7.4. UM $\rho <u'w'>$ (k) Zonal Wavenumber Spectra

We now consider the spectral distributions of MW momentum flux, their variations in altitude, and their dependence on UM spatial resolution. As above, these are averaged over the full UM domain and from 06 to 09 UT. Variations in altitude (Figure 15b) are explored with spectra at 30, 40, 50, and 58 km to avoid influences of the sponge layer at higher altitudes. The dominant contributions at all altitudes occur at λ_x ~ 100 km and smaller, despite the smaller contributions at larger λ_x exhibiting a peak at λ_x ~ 150 km.

These spectra reveal systematic reductions in MW MFs for λ_x < 200 km with each increase in altitude and with the reductions increasing strongly with decreasing λ_x. Specifically, spectral amplitudes decrease from 30 to 58 km by ~20% at λ_x = 50 km, ~90% at λ_x = 30 km, and ~100% at λ_x = 20 km. The larger reductions at decreasing λ_x are caused by MW reflections in the increasing U (z) with altitude, with larger λ_x reflecting at higher altitudes. As noted in section 4.2, λ_x ~ 40-km MWs will reflect near the peak U (z), while smaller λ_x MWs will reflect where c_{gz} = 0 or $\lambda_x \sim 2\pi U/N$. Hence, the spectral evolution in altitude has a clear physical basis.

Turning to the spectral variations with UM resolution (Figure 15c), we see decreases in MW momentum fluxes that vary strongly with k. Increasing Δx causes the mean MW wavelength to shift from λ_x ~ 50 km to ~150 km as Δx increases from 2 km to 32 km. At smaller λ_x, larger Δx, and likely coarser Δz than required, also strongly limit momentum fluxes.

8. Discussion

Early airborne and theoretical studies spanning more than six decades revealed the potential for MWs extending into the lower stratosphere and above under suitable propagation conditions (e.g., Bretherton, 1969; Lilly & Kennedy, 1973; Lilly, 1978; Schoeberl, 1985; McFarlane, 1987; and additional references cited by Grubišić & Lewis, 2004; Grubišić et al., 2008; and Fritts, Smith, et al., 2016). More recent airborne and modeling studies further advanced our understanding of MW penetration into, and effects in, the stratosphere and above (Bacmeister, 1993; Bacmeister & Gray, 1990; Bacmeister & Schoeberl, 1989; Doyle et al., 2005; Doyle et al., 2011; Sato et al., 2009; Sato et al., 2012; Satomura & Sato, 1999; R. B. Smith et al., 2008; Vosper, 2015; Vosper et al., 2016). Satellite measurements emphasized the frequent occurrence of, and contributions to mean temperature variances by, MWs in the winter stratosphere (Alexander et al., 2009; Alexander & Teitelbaum, 2007; Eckermann et al., 2007; Eckermann & Preusse, 1999; Hendricks et al., 2014; Jiang et al., 2002; Plougonven et al., 2008; Preusse et al., 2002).

Predictions of MWs in the mesosphere were first confirmed by ground-based airglow imaging over the Andes and NZ by S. Smith et al. (2009, 2013). These initial observations, and advancing lidar and imaging capabilities, were among the many scientific opportunities and open questions that motivated DEEPWAVE (Fritts, Smith, et al., 2016). To date, multiple DEEPWAVE studies have addressed a diversity of MW dynamics extending to altitudes of ~90 km and of their effects extending to higher altitudes (e.g., Bossert et al., 2015, 2017; Bramberger et al., 2017; Broutman et al.,

2017; Eckermann et al., 2016; Fritts, Smith, et al., 2016; Kaifler et al., 2015; Pautet et al., 2016). Similar MW and more general GW studies are now being performed using ground-based lidars, radars, and airglow imagers (e.g., Baumgarten et al., 2015; Hecht et al., 2018). To our knowledge, however, no other studies have approximated the capabilities of DEEPWAVE airborne measurements to quantify MW, and more general GW, horizontal and vertical scales, temporal variability, and their linear and nonlinear dynamics from ~0 to 100 km.

All DEEPWAVE flights addressing MW dynamics prior to 12 and 13 July were performed under relatively strong forcing conditions. However, ground-based measurements on 21 June revealed very strong MWs in the mesosphere over Lauder to the southeast of Mount Aspiring (see Figure 1, right) during weak forcing. These observations were a major motivation for RF22 on 12 and 13 July, during which decreasing cross-mountain flow was anticipated. In the 21 June case, the mean flow was toward the northeast and thus more nearly along than across the Southern Alps. The orography appears to have accounted for the MW scales (λ_x ~ 30–80 km) and alignments (N-S to NNW-SSE) seen in the mesosphere in that case (Fritts, Smith, et al., 2016; Figure 13). For example, see the ~30- to 80-km terrain features aligned roughly N-S to the south of Mount Cook in Figure 1. The weak forcing in that case also apparently enabled linear propagation and continuous amplitude growth with altitude into the mesosphere until decreasing U (z) in the upper mesosphere caused MW breaking (a ~ 1) beginning at ~75 km.

A second case of relatively weak forcing accompanied MWs excited by moderate flow over the low-orography Auckland Islands observed on RF23 performed on 14 July (e.g., Broutman et al., 2017; Eckermann et al., 2016; Pautet et al., 2016). MW propagation during RF23 exhibited strong horizontal dispersion due to the local source. This enabled linear Fourier ray modeling to describe the response extending into the upper mesosphere very well up to the point of MW breaking approaching a critical level observed in the GV AMTM and Na lidar measurements in the lee of the Auckland Islands.

These DEEPWAVE observations have revealed a previously unappreciated potential for strong MW forcing in the mesosphere when MW forcing is weak and strong stratospheric winds enable largely linear propagation to higher altitudes. In such cases, MW amplitudes and momentum deposition in the mesosphere can be appreciable and may extend over regions much larger than the underlying orography. These responses differ in significant ways from those under strong forcing conditions, in which MW responses are larger and more intermittent at lower altitudes, momentum deposition is implied throughout the atmospheric column, and secondary GWs play major roles at higher altitudes (e.g., Bossert et al., 2017; Bramberger et al., 2017).

9. Summary and Conclusions

Many studies of GW dynamics employing correlative measurements have made significant contributions to our understanding over many years. In the majority of cases, however, these studies were confined in altitude and did not link GW sources with their effects at higher altitudes. Even fewer were able to define GW horizontal and vertical scales, orientations, intrinsic properties, and consequences of GW breaking spanning multiple GW periods. DEEPWAVE overcame these obstacles through comprehensive, full-column measurements where MW responses were confined to the same region throughout their event durations.

Results for the DEEPWAVE RF22 event presented in this paper reveal largely linear excitation of vertically propagating MWs and trapped lee waves accompanying weak flow over the complex SI orography spanning 12–13 July 2014. MWs at λ_h ~ 20–300 km readily reached the upper stratosphere with significant amplitudes, though potentially exhibiting localized dissipation at lower altitudes where λ_z and c_{gz} were very small due to weak, decreasing, or nearly uniform U (z).

MWs having $\lambda_h < 40$ km apparently became evanescent and reflected near the U (z) maximum at ~55–60 km, thus limiting the amplitudes of these MWs at higher altitudes. Larger-λ_h MWs that propagated into the mesosphere achieved overturning amplitudes at ~75–84 km, implying strong breaking and instabilities, secondary GW generation (e.g., Bossert et al., 2015, 2017), and MW dissipation below a critical level near 90 km. Peak-to-peak vertical displacements accompanying these dynamics exceeded 10 km on every RF22 flight leg. Estimated displacements and related T' for the larger individual MWs led to momentum flux estimates of 310, 410, and 690 m^2/s^2, which are a decade or more larger than zonal mean magnitudes at these altitudes.

UM simulations of this event capture many of the characteristics of the observed MW field throughout the atmosphere, in particular, the dominant scales, orientations, and spatial and temporal variability. They also suggest that the major momentum fluxes (~70%) occur at $\lambda_x < 100$ km, despite dominance of the T' and u' fields by MWs at larger scales. However, the UM significantly underestimates MW amplitudes at all altitudes and was unable to replicate large observed $\lambda_x \sim 300$ km seen by AIRS at 43 km at 03:19 UT on 13 July. We attribute this to very small λ_z and c_{gz} following a UM initialization at 12 UT on 12 July.

The implications of this study are that linear MW propagation into the mesosphere can occur when forcing is weak and there is a suitable propagation channel to high altitudes. In such cases, momentum fluxes can become very large in the mesosphere and may extend over a region significantly larger than the forcing orography. This differs significantly from other DEEPWAVE cases where either strong forcing or weak stratospheric winds drive initial MW breaking and momentum deposition at much lower altitudes.

These and other DEEPWAVE results have significant implications for parameterizations of MW and more general GW propagation and influences throughout the atmospheric column (e.g., Bossert et al., 2015, 2017; Bramberger et al. (2017); Eckermann et al. (2016); Fritts, Smith, et al. (2016); Kaifler et al. (2015); Pautet et al. (2016); R. B. Smith et al. (2016). These include the following:

1. Orographic forcing often yields multiple MW scales and orientations, and the dominant responses often have primary k_h along the cross-mountain flow.
2. Horizontal dispersion leads to extended horizontal responses and forcing in the stratosphere and mesosphere that violate the typical general circulation model single-column approximation.
3. Small λ_z and c_{gz} where $(c - U_h)$ is small can delay high-altitude responses by many hours.
4. The linear view of GW breaking is wrong: Breaking is intermittent, it does not eliminate the GW, and the GW can again achieve large amplitudes at higher altitudes.
5. Even when larger-scale ($\lambda_h \sim 100$–300 km) MWs are observed, the major momentum fluxes are typically associated with $\lambda_h < 100$ km.

Acknowledgments
Research described here was performed under NSF and ONR grants or contracts cited in GEMS. Generation of NAVGEM reanalyses was made possible by resources from the DoD High Performance Computer Modernization Program. We thank the many participants in the DEEPWAVE program for their contributions in enabling the measurements analyzed here and personnel maintaining the DEEPWAVE data archive at NCAR/EOL available at https://www.eol.ucar.edu/field_projects/deepwave, where interested parties can access the DEEPWAVE data. We also thank three anonymus reviewers for valuable comments on the manuscript.

References

Alexander, M. J., Eckermann, S. D., Broutman, D., & Ma, J. (2009). Momentum flux estimates for South Georgia Island mountain waves in the stratosphere observed via satellite. *Geophysical Research Letters*, *36*, L12816. https://doi.org/10.1029/2009GL038587

Alexander, M. J., & Teitelbaum, H. (2007). Observation of a large amplitude mountain wave event over the Antarctic Pennisula. *Journal of Geophysical Research*, *112*, D21103. https://doi.org/10.1029/2006JD008368

Bacmeister, J. T. (1993). Mountain wave drag in the stratosphere and mesosphere inferred from observed winds and a simple mountain-wave parameterization scheme. *Journal of the Atmospheric Sciences*, *50*(3), 377–399. https://doi.org/10.1175/1520-0469(1993)050<0377:MWDITS>2.0.CO;2

Bacmeister, J. T., & Gray, B. (1990). ER-2 mountain wave encounter over Antarctica: Evidence for blocking. *Geophysical Research Letters*, *17*(1), 81–84. https://doi.org/10.1029/GL017i001p00081

Bacmeister, J. T., & Schoeberl, M. R. (1989). Breakdown of vertically propagating two-dimensional gravity waves forced by orography. *Journal of the Atmospheric Sciences*, *46*(14), 2109–2134. https://doi.org/10.1175/1520-0469(1989)046<2109:BOVPTD>2.0.CO;2

Baumgarten, G., Fiedler, J., Hildebrand, J., & Lübken, F.-J. (2015). Inertia gravity wave in the stratosphere and mesosphere observed by Doppler wind and temperature lidar. *Geophysical Research Letters*, *42*, 10,929–10,936. https://doi.org/10.1002/2015GL066991

Bossert, K., Fritts, D. C., Heale, C. J., Eckermann, S. D., Plane, J. M. C., Snively, J. B., et al. (2018). Momentum flux spectra of a mountain wave event over New Zealand. *Journal of Geophysical Research: Atmospheres*, *123*. https://doi.org/10.1029/2018JD028319

Bossert, K., Fritts, D. C., Pautet, P.-D., Williams, B. P., Taylor, M. J., Kaifler, B., et al. (2015). Momentum flux estimates accompanying multiscale gravity waves over Mount Cook, New Zealand, on 13 July 2014 during the DEEPWAVE campaign. *Journal of Geophysical Research*, *120*, 9323–9337. https://doi.org/10.1002/2015JD023197

Bossert, K., Kruse, C. G., Heale, C. J., Fritts, D. C., Williams, B. P., Snively, J. B., et al. (2017). Secondary gravity wave generation over New Zealand during the DEEPWAVE campaign. *Journal of Geophysical Research: Atmospheres*, *122*, 7834–7850. https://doi.org/10.1002/2016JD026079

Bougeault, P., Binder, P., Buzzi, A., Dirks, R., Kuettner, J., Houze, R., et al. (2001). The MAP special observing period. *Bulletin of the American Meteorological Society*, *82*(3), 433–462. https://doi.org/10.1175/1520-0477

Bramberger, M., Dörnbrack, A., Bossert, K., Ehard, B., Fritts, D. C., Kaifler, B., et al. (2017). Does strong tropospheric forcing cause large-amplitude mesospheric gravity waves?—A DEEPWAVE case study. *Journal of Geophysical Research: Atmospheres*, *122*, 11,422–11,443. https://doi.org/10.1002/2017JD027371

Bretherton, F. P. (1969). Momentum transport by gravity waves. *Quarterly Journal of the Royal Meteorological Society*, *95*(404), 213–243. https://doi.org/10.1002/qj.49709540402

Broutman, D., Eckermann, S. D., Knight, H., & Ma, J. (2017). A stationary phase solution for mountain waves with application to mesospheric mountain waves generated by Auckland Island. *Journal of Geophysical Research: Atmospheres*, *122*, 699–711. https://doi.org/10.1002/2016JD025699

Bühler, O. (2014). *Waves and mean flows*. Cambridge: Cambridge University Press.

Bühler, O., McIntyre, M. E., & Scinocca, J. F. (1999). On shear-generated gravity waves that reach the mesosphere. Part I: Wave generation. *Journal of the Atmospheric Sciences*, *56*(21), 3749–3763. https://doi.org/10.1175/1520-0469(1999)056<3749:OSGGWT>2.0.CO;2

Chimonas, G., & Grant, J. R. (1984). Shear excitation of gravity waves. Part II: Upscale scattering from Kelvin-Helmholtz waves. *Journal of the Atmospheric Sciences*, *41*(15), 2278–2288. https://doi.org/10.1175/1520-0469(1984)041<2278:SEOGWP>2.0.CO;2

Dong, B., & Yeh, K. C. (1988). Resonant and nonresonant wave-wave interactions in an isothermal atmosphere. *Journal of Geophysical Research*, *93*(D4), 3729–3744. https://doi.org/10.1029/JD093iD04p03729

Dosser, H. V., & Sutherland, B. R. (2011). Weakly nonlinear non-Boussinesq internal gravity wavepackets. *Physica D*, *240*(3), 346–356. https://doi.org/10.1016/j.physd.2010.09.008

Doyle, J. D., Gaberšek, S., Jiang, Q., Bernardet, L., Brown, J. M., Dörnbrack, A., et al. (2011). An intercomparison of T-REX mountain-wave simulations and implications for mesoscale predictability. *Monthly Weather Review*, *139*(9), 2811–2831. https://doi.org/10.1175/MWR-D-10-05042.1

Doyle, J. D., Shapiro, M., Jiang, Q., & Bartels, D. (2005). Large-amplitude mountain wave breaking over Greenland. *Journal of the Atmospheric Sciences*, *62*(9), 3106–3126. https://doi.org/10.1175/JAS3528.1

Dunkerton, T. J. (1989). Theory of internal gravity wave saturation. *Pure and Applied Geophysics*, *130*, 373–397.

Durran, D. R. (1990). Mountain waves and downslope winds, atmospheric processes over complex terrain. *Meteorological Monographs*, *23*(45), 59–83.

Eckermann, S. D., Broutman, D., Ma, J., Doyle, J. D., Pautet, P.-D., Taylor, M. J., et al. (2016). Dynamics of orographic gravity waves observed in the mesosphere over the Auckland Islands during the Deep Propagating Gravity Wave Experiment (DEEPWAVE). *Journal of the Atmospheric Sciences*, *73*(10), 3855–3876. https://doi.org/10.1175/JAS-D-16-0059.1

Eckermann, S. D., Ma, J., Hoppel, K. W., Kuhl, D. D., Allen, D. R., Doyle, J. A., et al. (2018). High-altitude (0–100 km) global atmospheric reanalysis system: Description and application to the 2014 austral winter of the Deep Propagating Gravity-Wave Experiment (DEEPWAVE). *Monthly Weather Review*, *146*(8), 2639–2666. https://doi.org/10.1175/MWR-D-17-0386.1

Eckermann, S. D., Ma, J., & Wu, D. L. (2007). A three-dimensional mountain wave imaged in satellite radiance throughout the stratosphere: Evidence of the effects of directional wind shear. *Quarterly Journal of the Royal Meteorological Society*, *133*(629), 1959–1975. https://doi.org/10.1002/qj.187

Eckermann, S. D., & Preusse, P. (1999). Global measurements of stratospheric mountain waves from space. *Science*, *286*(5444), 1534–1537. https://doi.org/10.1126/science.286.5444.1534

Eliassen, A., & Palm, E. (1961). On the transfer of energy in stationary mountain waves. *Geophysics Publications*, *22*, 1–23.

Fovell, R., Durran, D., & Holton, J. R. (1992). Numerical simulations of convectively generated stratospheric gravity waves. *Journal of the Atmospheric Sciences*, *49*(16), 1427–1442. https://doi.org/10.1175/1520-0469(1992)049<1427:NSOCGS>2.0.CO;2

Fritts, D. C. (1984). Shear excitation of atmospheric gravity waves. Part II: Nonlinear radiation from a free shear layer. *Journal of the Atmospheric Sciences*, *41*(4), 524–537.

Fritts, D. C., & Alexander, M. J. (2003). Gravity dynamics and effects in the middle atmosphere. *Reviews of Geophysics*, *41*(1), 1003. https://doi.org/10.1029/2001RG000106

Fritts, D. C., Laughman, B., Lund, T. S., & Snively, J. B. (2015). Self-acceleration and instability of gravity wave packets: 1. Effects of temporal localization. *Journal of Geophysical Research: Atmospheres*, *120*, 8783–8803. https://doi.org/10.1002/2015JD023363

Fritts, D. C., Laughman, B., Wang, L., Lund, T., & Collins, R. L. (2018). Gravity wave dynamics in a mesospheric inversion layer: 1. Reflection, trapping, and instability dynamics. *Journal of Geophysical Research: Atmospheres*, *123*, 626–648. https://doi.org/10.1002/2017JD027440

Fritts, D. C., & Nastrom, G. D. (1992). Sources of mesoscale variability of gravity waves, II, frontal, convective, and jet stream excitation. *Journal of the Atmospheric Sciences*, *49*(2), 111–127. https://doi.org/10.1175/1520-0469(1992)049<0111:SOMVOG>2.0.CO;2

Fritts, D. C., & Rastogi, P. K. (1985). Convective and dynamical instabilities due to gravity wave motions in the lower and middle atmosphere: Theory and observations. *Radio Science*, *20*(6), 1247–1277. https://doi.org/10.1029/RS020i006p01247

Fritts, D. C., Smith, R. B., Taylor, M. J., Doyle, J. D., Eckermann, S. D., Dörnbrack, A., et al. (2016). The Deep Propagating Gravity Wave Experiment (DEEPWAVE): An airborne and ground-based exploration of gravity wave propagation and effects from their sources throughout the lower and middle atmosphere. *Bulletin of the American Meteorological Society*, *97*(3), 425–453. https://doi.org/10.1175/BAMS-D-14-00269.1

Fritts, D. C., Wang, L., Baumgarten, G., Miller, A. D., Geller, M. A., Jones, G., et al. (2017). High-resolution observations and modeling of turbulence sources, structures, and intensities in the upper mesosphere. *Journal of Atmospheric and Solar - Terrestrial Physics*, *162*, 57–78. https://doi.org/10.1016/j.jastp.2016.11.006

Fritts, D. C., Wang, L., Geller, M. A., Lawrence, D. A., Werne, J., & Balsley, B. B. (2016). Numerical modeling of multi-scale dynamics at a high Reynolds number: Instabilities, turbulence, and an assessment of Ozmidov and Thorpe scales. *Journal of the Atmospheric Sciences*, *73*(2), 555–578. https://doi.org/10.1175/JAS-D-14-0343.1

Fritts, D. C., Wang, L., Werne, J., Lund, T., & Wan, K. (2009a). Gravity wave instability dynamics at high Reynolds numbers, 1: Wave field evolution at large amplitudes and high frequencies. *Journal of the Atmospheric Sciences*, *66*(5), 1126–1148. https://doi.org/10.1175/2008JAS2726.1

Fritts, D. C., Wang, L., Werne, J., Lund, T., & Wan, K. (2009b). Gravity wave instability dynamics at high Reynolds numbers, 2: Turbulence evolution, structure, and anisotropy. *Journal of the Atmospheric Sciences*, *66*(5), 1149–1171. https://doi.org/10.1175/2008JAS2727.1

Fritts, D. C., Wang, L., & Werne, J. A. (2013). Gravity wave-fine structure interactions. Part I: Influences of fine structure form and orientation on flow evolution and instability. *Journal of the Atmospheric Sciences*, *70*(12), 3710–3734. https://doi.org/10.1175/JAS-D-13-055.1

Grimshaw, R. (1988). Resonant wave interactions in a stratified shear flow. *Journal of Fluid Mechanics*, *190*(1), 357–374. https://doi.org/10.1017/S0022112088001351

Grubišić, V., Doyle, J. D., Kuettner, J., Dirks, R., Cohn, S. A., Pan, L. L., et al. (2008). The Terrain-Induced Rotor Experiment. *Bulletin of the American Meteorological Society*, *89*(10), 1513–1534. https://doi.org/10.1175/2008BAMS2487.1

Grubišić, V., & Lewis, J. M. (2004). Sierra Wave Project revisited: 50 years later. *Bulletin of the American Meteorological Society*, *85*(8), 1127–1142. https://doi.org/10.1175/BAMS-85-8-1127

Guest, F. M., Reeder, M. J., Marks, C. J., & Karoly, D. J. (2000). Inertia-gravity waves observed in the lower stratosphere over Macquarie Island. *Journal of the Atmospheric Sciences*, *57*(5), 737–752. https://doi.org/10.1175/1520-0469(2000)057<0737:IGWOIT>2.0.CO;2

Heale, C. J., Bossert, K., Snively, J. B., Fritts, D. C., Pautet, P.-D., & Taylor, M. J. (2017). Numerical modeling of a multiscale gravity wave event and its airglow signatures over Mount Cook, New Zealand, during the DEEPWAVE campaign. *Journal of Geophysical Research: Atmospheres*, *122*, 846–860. https://doi.org/10.1002/2016JD025700

Hecht, J. H., Fritts, D. C., Wang, L., Gelinas, L. J., Rudy, R. J., Walterscheid, R. L., & Franke, S. J. (2018). Observations of the breakdown of mountain waves over the Andes Lidar Observatory at Cerro Pachon on 8/9 July 2012. *Journal of Geophysical Research: Atmospheres*, *123*, 276–299. https://doi.org/10.1002/2017JD027303

Hendricks, E. A., Doyle, J. D., Eckermann, S. D., Jiang, Q., & Alex Reinecke, P. (2014). What is the source of the stratospheric gravity wave belt in austral winter? *Journal of the Atmospheric Sciences*, *71*(5), 1583–1592. https://doi.org/10.1175/JAS-D-13-0332.1

Hines, C. O. (1991). The saturation of gravity waves in the middle atmosphere. Part II: Development of Doppler-spread theory. *Journal of the Atmospheric Sciences*, *48*(11), 1361–1379. https://doi.org/10.1175/1520-0469(1991)048<1361:TSOGWI>2.0.CO;2

Hirota, I., & Niki, T. (1985). A statistical study of inertia-gravity waves in the middle atmosphere. *Journal of the Meteorological Society of Japan*, *63*(6), 1055–1066. https://doi.org/10.2151/jmsj1965.63.6_1055

Horinouchi, T., Nakamura, T., & Kosaka, J.-I. (2002). Convectively generated mesoscale gravity waves simulated throughout the middle atmosphere. *Geophysical Research Letters*, *29*(21), 2007. https://doi.org/10.1029/2002GL016069

Huang, K. M., Zhang, S. D., & Yi, F. (2007). A numerical study on nonresonant interactions of gravity waves in a compressible atmosphere. *Journal of Geophysical Research*, *112*, D11115. https://doi.org/10.1029/2006JD007373

Huang, K. M., Zhang, S. D., & Yi, F. (2009). Gravity wave excitation through resonant interaction in a compressible atmosphere. *Geophysical Research Letters*, *36*, L01803. https://doi.org/10.1029/2008GL035575

Huang, K. M., Zhang, S. D., & Yi, F. (2011). Atmospheric gravity wave excitation through sum nonresonant interaction. *Journal of Atmospheric and Solar - Terrestrial Physics*, *73*(17-18), 2429–2436. https://doi.org/10.1016/j.jastp.2011.09.009

Jiang, J. H., Wu, D. L., & Eckermann, S. D. (2002). Upper Atmosphere Research Satellite (UARS) observation of mountain waves over the Andes. *Journal of Geophysical Research*, *107*(D20), 8273. https://doi.org/10.1029/2002JD002091

Jiang, J. H., Wu, D. L., Eckermann, S. D., & Ma, J. (2003). Mountain waves in the middle atmosphere: Microwave limb sounder observations and analyses. *Advances in Space Research*, *32*(5), 801–806. https://doi.org/10.1016/S0273-1177(03)00402-2

Kaifler, B., Kaifler, N., Ehard, B., D.rnbrack, A., Rapp, M., & Fritts, D. C. (2015). Influences of source conditions on mountain wave penetration into the stratosphere and mesosphere. *Geophysical Research Letters*, *42*, 9488–9494. https://doi.org/10.1002/2015GL066465

Klemp, J. B., & Lilly, D. K. (1978). Numerical simulation of hydrostatic mountain waves. *Journal of the Atmospheric Sciences*, *35*(1), 78–107. https://doi.org/10.1175/1520-0469(1978)035<0078:NSOHMW>2.0.CO;2

Klostermeyer, J. (1991). Two and three-dimensional parametric instabilities in finite amplitude internal gravity waves. *Geophysical and Astrophysical Fluid Dynamics*, *61*(1-4), 1–25. https://doi.org/10.1080/03091929108229035

Kruse, C. G., & Smith, R. B. (2015). Gravity wave diagnostics and characteristics in mesoscale fields. *Journal of the Atmospheric Sciences*, *72*(11), 4372–4392. https://doi.org/10.1175/JAS-D-15-0079.1

Lane, T. P., Reeder, M. J., & Clark, T. L. (2001). Numerical modeling of gravity wave generation by deep tropical convection. *Journal of the Atmospheric Sciences*, *58*(10), 1249–1274. https://doi.org/10.1175/1520-0469(2001)058<1249:NMOGWG>2.0.CO;2

Lelong, M.-P., & Dunkerton, T. J. (1998). Inertia–gravity wave breaking in three dimensions. Part I: Convectively stable waves. *Journal of the Atmospheric Sciences*, *55*, 2473–2488.

Lilly, D. K. (1978). A severe downslope windstorm and aircraft turbulence induced by a mountain wave. *Journal of the Atmospheric Sciences*, *35*(1), 59–77. https://doi.org/10.1175/1520-0469(1978)035<0059:ASDWAA>2.0.CO;2

Lilly, D. K., & Kennedy, P. J. (1973). Observations of a stationary mountain wave and its associated momentum flux and energy dissipation. *Journal of the Atmospheric Sciences*, *30*(6), 1135–1152. https://doi.org/10.1175/1520-0469(1973)030<1135:OOASMW>2.0.CO;2

Lilly, D. K., & Lester, P. F. (1974). Waves and turbulence in the stratosphere. *Journal of the Atmospheric Sciences*, *31*(3), 800–812. https://doi.org/10.1175/1520-0469(1974)031<0800:WATITS>2.0.CO;2

Liu, H.-L., McInerney, J. M., Santos, S., Lauritzen, P. H., Taylor, M. A., & Pedatella, N. M. (2014). Gravity waves simulated by high-resolution Whole Atmosphere Community Climate Model. *Geophysical Research Letters*, *41*, 9106–9112. https://doi.org/10.1002/2014GL062468

Lombard, P. N., & Riley, J. J. (1996). Instability and breakdown of internal gravity waves. I. Linear stability analysis. *Physics of Fluids*, *8*(12), 3271–3287. https://doi.org/10.1063/1.869117

McComas, C. H., & Bretherton, F. P. (1977). Resonant interaction of oceanic internal waves. *Journal of Geophysical Research*, *82*(9), 1397–1412. https://doi.org/10.1029/JC082i009p01397

McFarlane, N. A. (1987). The effect of orographically excited gravity wave drag on the general circulation of the lower stratosphere and troposphere. *Journal of the Atmospheric Sciences*, *44*(14), 1775–1800. https://doi.org/10.1175/1520-0469(1987)044<1775:TEOOEG>2.0.CO;2

Nappo, C. J. (2002). *An introduction to atmospheric atmospheric gravity waves*, *International Geophysics Series* (Vol. 85, 276 pp.). San Diego, CA: Academic Press.

Nastrom, G. D., & Fritts, D. C. (1992). Sources of mesoscale variability of gravity waves, I: Topographic excitation. *Journal of the Atmospheric Sciences*, *49*(2), 101–110. https://doi.org/10.1175/1520-0469(1992)049<0101:SOMVOG>2.0.CO;2

Pautet, P.-D., Taylor, M. J., Fritts, D. C., Bossert, K., Williams, B. P., Broutman, D., et al. (2016). Large-amplitude mesospheric response to an orographic wave generated over the Southern Ocean Auckland Islands (50.7°S) during the DEEPWAVE project. *Journal of Geophysical Research: Atmospheres*, *121*, 1431–1441. https://doi.org/10.1002/2015JD024336

Pfister, L., Scott, S., Loewenstein, M., Bowen, S., & Legg, M. (1993). Mesoscale disturbances in the tropical stratosphere excited by convection: Observations and effects on the stratospheric momentum budget. *Journal of the Atmospheric Sciences*, *50*(8), 1058–1075. https://doi.org/10.1175/1520-0469(1993)050<1058:MDITTS>2.0.CO;2

Plougonven, R., Hertzog, A., & Teitelbaum, H. (2008). Observations and simulations of a large-amplitude mountain wave breaking over the Antarctic Peninsula. *Journal of Geophysical Research*, *113*, D16113. https://doi.org/10.1029/2007JD009739

Plougonven, R., & Snyder, C. (2007). Inertia–gravity waves spontaneously generated by jets and fronts. Part I: Different baroclinic life cycles. *Journal of the Atmospheric Sciences*, *64*(7), 2502–2520. https://doi.org/10.1175/JAS3953.1

Plougonven, R., & Zhang, F. (2014). Internal gravity waves from atmospheric jets and fronts. *Reviews of Geophysics*, *52*, 33–76. https://doi.org/10.1002/2012RG000419

Preusse, P., Dornbrack, A., Eckermann, S. D., Riese, M., Schaeler, B., Bacmeister, J. T., et al. (2002). Space-based measurements of stratospheric mountain waves by CRISTA: 1. Sensitivity, analysis method, and a case study. *Journal of Geophysical Research*, *107*(D23), 8178. https://doi.org/10.1029/2001JD000699

Sato, K., Tateno, S., Watanabe, S., & Kawatani, Y. (2012). Gravity wave characteristics in the Southern Hemisphere revealed by a high-resolution middle-atmosphere general circulation model. *Journal of the Atmospheric Sciences*, *69*(4), 1378–1396. https://doi.org/10.1175/JAS-D-11-0101.1

Sato, K., Watanabe, S., Kawatani, Y., Tomikawa, Y., Miyazaki, K., & Takahashi, M. (2009). On the origins of mesospheric gravity waves. *Geophysical Research Letters*, *36*, L19801. https://doi.org/10.1029/2009GL039908

Satomura, T., & Sato, K. (1999). Secondary generation of gravity waves associated with the breaking of mountain waves. *Journal of the Atmospheric Sciences*, *56*(22), 3847–3858. https://doi.org/10.1175/1520-0469(1999)056<3847:SGOGWA>2.0.CO;2

Schoeberl, M. R. (1985). The penetration of mountain waves into the middle atmosphere. *Journal of the Atmospheric Sciences*, *42*(24), 2856–2864. https://doi.org/10.1175/1520-0469(1985)042<2856:TPOMWI>2.0.CO;2

Scinocca, J. F., & Ford, R. (2000). The nonlinear forcing of large-scale internal gravity waves by stratified shear instability. *Journal of the Atmospheric Sciences*, *57*(5), 653–672. https://doi.org/10.1175/1520-0469(2000)057<0653:TNFOLS>2.0.CO;2

Shutts, G. J., & Vosper, S. B. (2011). Stratospheric gravity waves revealed in NWP model forecasts. *Quarterly Journal of the Royal Meteorological Society*, *137*, 303–317.

Smith, R. B., Doyle, J. D., Jiang, Q., & Smith, S. A. (2007). Alpine gravity waves: Lessons from MAP regarding mountain wave generation and breaking. *Quarterly Journal of the Royal Meteorological Society*, *133*(625), 917–936. https://doi.org/10.1002/qj.103

Smith, R. B., Nugent, A. D., Kruse, C. G., Fritts, D. C., Doyle, J. D., Eckermann, S. D., et al. (2016). Stratospheric gravity wave fluxes and scales during DEEPWAVE. *Journal of the Atmospheric Sciences*, *73*(7), 2851–2869. https://doi.org/10.1175/JAS-D-15-0324.1

Smith, R. B., Woods, B. K., Jensen, J., Cooper, W. A., Doyle, J. D., Jiang, Q. F., & Grubisic, V. (2008). Mountain waves entering the stratosphere. *Journal of the Atmospheric Sciences*, *65*(8), 2543–2562. https://doi.org/10.1175/2007JAS2598.1

Smith, S., Baumgardner, J., & Mendillo, M. (2009). Evidence of mesospheric gravity-waves generated by orographic forcing in the troposphere. *Geophysical Research Letters*, *36*, L08807. https://doi.org/10.1029/2008GL036936

Smith, S. M., Vadas, S. L., Baggaley, W. J., Hernandez, G., & Baumgardner, J. (2013). Gravity wave coupling between the mesosphere and thermosphere over New Zealand. *Journal of Geophysical Research*, *118*, 2694–2707. https://doi.org/10.1002/jgra.50263

Sonmor, L. J., & Klaassen, G. P. (1997). Toward a unified theory of gravity wave stability. *Journal of the Atmospheric Sciences*, *54*(22), 2655–2680. https://doi.org/10.1175/1520-0469(1997)054<2655:TAUTOG>2.0.CO;2

Staquet, C., & Sommeria, J. (2002). Internal gravity waves: From instabilities to turbulence. *Annual Review of Fluid Mechanics*, *34*(1), 559–593. https://doi.org/10.1146/annurev.fluid.34.090601.130953

Sutherland, B. R. (2006a). Internal wave instability: Wave-wave versus wave-induced mean flow interactions. *Physics of Fluids*, *18*(7), 074107. https://doi.org/10.1063/1.2219102

Sutherland, B. R. (2006b). Weakly nonlinear internal gravity wave packets. *Journal of Fluid Mechanics*, *569*, 249–258. https://doi.org/10.1017/S0022112006003016

Sutherland, B. R. (2010). *Internal gravity waves*. Cambridge: Cambridge University Press.

Thomas, L., Prichard, I. T., & Astin, I. (1992). Radar observations of an inertia-gravity wave in the troposphere and lower stratosphere. *Annales de Geophysique*, *10*, 690–697.

Tsuda, T., Nishida, M., & Rocken, C. (2000). A global morphology of gravity wave activity in the stratosphere revealed by the GPS occultation data (GPS/MET). *Journal of Geophysical Research*, *105*(D6), 7257–7273. https://doi.org/10.1029/1999JD901005

Uccellini, L. W., & Koch, S. E. (1987). The synoptic setting and possible energy sources for mesoscale wave disturbances. *Monthly Weather Review*, *115*(3), 721–729. https://doi.org/10.1175/1520-0493(1987)115<0721:TSSAPE>2.0.CO;2

Vadas, S. L. (2007). Horizontal and vertical propagation, and dissipation of gravity waves in the thermosphere from lower atmospheric and thermospheric sources. *Journal of Geophysical Research*, *112*, A06305. https://doi.org/10.1029/2006JA011845

Vadas, S. L., & Fritts, D. C. (2001). Gravity wave radiation and mean responses to local body forces in the atmosphere. *Journal of the Atmospheric Sciences*, *58*, 2249–2279.

Vanneste, J. (1995). The instability of internal gravity waves to localized disturbances. *Annales de Geophysique*, *13*(2), 196–210. https://doi.org/10.1007/s00585-995-0196-7

Vosper, S. B. (2015). Mountain waves and wakes generated by South Georgia: Implications for drag parametrization. *Quarterly Journal of the Royal Meteorological Society*, *141*(692), 2813–2827. https://doi.org/10.1002/qj.2566

Vosper, S. B., Brown, A. R., & Webster, S. (2016). Orographic drag on islands in the NWP mountain grey zone. *Quarterly Journal of the Royal Meteorological Society*, *142*(701), 3128–3137. https://doi.org/10.1002/qj.2894

Wu, D. L., & Eckermann, S. D. (2008). Global gravity wave variances from Aura MLS: Characteristics and interpretation. *Journal of the Atmospheric Sciences*, *65*(12), 3695–3718. https://doi.org/10.1175/2008JAS2489.1

Yeh, K. C., & Liu, C. H. (1981). The instability of atmospheric gravity waves through wave-wave interactions. *Journal of Geophysical Research*, *86*(C10), 9722–9728. https://doi.org/10.1029/JC086iC10p09722

Yue, J., Vadas, S. L., She, C.-Y., Nakamura, T., Reising, S., Krueger, D., et al. (2009). A study of OH imager observed concentric gravity waves near Fort Collins on 11 May 2004. *Journal of Geophysical Research*, *114*, D06104. https://doi.org/10.1029/2008JD011244

Zhang, F. (2004). Generation of mesoscale gravity waves in upper-tropospheric jet–front systems. *Journal of the Atmospheric Sciences*, *61*(4), 440–457. https://doi.org/10.1175/1520-0469(2004)061<0440:GOMGWI>2.0.CO;2